Impact of assimilating adaptively thinned AIRS cloud-cleared radiances on the analysis of Polar Lows and Mediterranean Sea Tropical-like Cyclone in a global modeling and data assimilation framework

Manisha Ganeshan*

Climate and Radiation Laboratory, NASA Goddard Space Flight Center, Greenbelt, and Morgan State University, Baltimore, Maryland

Oreste Reale

Science Systems and Applications, Inc., Lanham, Maryland, and Global Modeling and Assimilation Office, NASA Goddard Space Flight Center, Greenbelt, Maryland

Erica McGrath-Spangler and Niama Boukachaba

Global Modeling and Assimilation Office, NASA Goddard Space Flight Center, Greenbelt, and Morgan State University, Baltimore, Maryland

Corresponding author: Manisha Ganeshan, manisha.ganeshan@nasa.gov

ABSTRACT

Polar Lows, and mesoscale convective cyclones bearing resemblance to Tropical Cyclones but originating outside of the tropics, are storms that are challenging to represent accurately in global analyses and models because of their small size, rapid growth at sub-synoptic scales, occurrence in data poor oceanic regions, and difficulties in objectively validating them in analysis. Building on previous positive results obtained with respect to the representation of Tropical Cyclones (TCs) in a global model, a set of observing system experiments (OSEs) performed using the NASA Goddard Earth Observing System (GEOS, version 5) are investigated, focusing on three case studies – a polar low in the Sea of Okhotsk, a polar low in the Southern Ocean, and a Mediterranean Sea tropical-like cyclone that occurred during the boreal fall season of 2014. Experiments assimilating adaptively thinned cloud-cleared hyperspectral infrared radiances from the Atmospheric InfraRed Sounder (AIRS) instrument onboard the NASA Aqua satellite, with higher density in the vicinity of each storm and its pre-cyclogenesis environment, and lower density elsewhere, demonstrate a positive impact on the analyzed representation of each storm. The adaptive thinning experiments improve the storm intensity and structure, including vertical alignment, depth, symmetry, strength and compactness of warm core compared to the reference experiments. The results suggest that jet-level processes associated with extremely strong horizontal velocity gradients as represented in the model analysis can be useful to locate dynamically active regions of the extratropical atmosphere where denser data coverage is likely to improve the analyzed representation of polar lows and other similar marine mesoscale convective cyclones.

Significance statement. Extratropical maritime mesoscale convective cyclones are short-lived, elusive features that are difficult to represent accurately in global analyses. Previous work by this team demonstrated a positive impact of an adaptive thinning methodology for infrared radiances applied to the Tropical Cyclone (TC) analysis. The methodology allows a relatively greater volume of radiance data to be assimilated around TCs within a TC-centered moving domain in a global model, yielding an improvement in TC structure and intensity forecast. A similar approach is explored here for two Polar Lows and a Mediterranean Sea Tropical-like Cyclone, wherein infrared radiances are more densely assimilated in the vicinity of each storm and its pre-cyclogenesis environment, resulting in a positive impact on the representation of the storm. Strong jet-level horizontal velocity gradients appear to precede each storm, and could be used to automate the adaptive thinning strategy in the future.

1. Introduction

a. Polar Lows and marine mesoscale tropical-like cyclones

Polar Lows (PLs) are meso-α-scale cyclones that form over high latitude ice-free ocean, fueled by the exchange of turbulent heat fluxes. They may be associated with gale force winds, intense precipitation, high waves, and freezing sea-spray, posing a severe threat to maritime vessels. PLs have a small *warm core* sustained by moist convection over ocean that is often nested in a larger-scale cold anomaly, distinguishing them from standard midlatitude baroclinic cyclones. In this regard, they are similar to tropical cyclones (TCs) albeit occurring over relatively colder seas and associated with much shorter lifecycles. Emanuel and Rotunno (1989) confirmed through numerical experiments that intense TC like storms can indeed develop in the high latitude ocean environment, referring to such storms as "Arctic Hurricanes". Similarities have also been drawn

between PLs and Mediterranean Sea Tropical-like cyclones (T-LCs) alternatively referred to as "Medicanes" (Rasmussen and Zick 1987; Businger and Reed 1989; Reale and Atlas 2001; Tous et al. 2013; Romero and Emanuel 2016; Mazza et al. 2017; Miglietta et al. 2017; Pytharoulis 2018; Almazroui et al. 2018; Miglietta and Rotunno 2019). PLs and Mediterranean Sea T-LCs represent two examples of a continuum of convectively-driven mesoscale cyclones that form over ice-free waters outside of the tropics, evolving from or into baroclinically driven disturbances (Hart 2003).

High latent and sensible heat flux totals from the ocean surface, typically on the order of $500 W\,m^{-2}$ or greater, are necessary for tropical cyclone development and maintenance. Fluxes of comparable magnitude can also exist in high latitudes, often in association with strong air-sea temperature differences consequent to cold polar continental or Arctic air outbreaks over relatively warm and ice-free ocean, although the ratio between sensible and latent heat flux is larger than in the tropics. As with TCs, enhanced surface heat fluxes establish a favorable environment for moist adiabatic instability and convection, but are not sufficient for PL cyclogenesis. Pre-existing baroclinic instability that may be associated with synoptic forcings such as cold upper troughs or cut-off lows (Businger and Reed 1989; Rasmussen and Cederskov 1994; Rasmussen et al. 1996; Parker and Hudson 1991; Noer and Ovhed 2003), is often the source of cyclonic vorticity associated with PL development (Harrold and Browning 1969; Reed and Duncan 1987; Reed 1979; Sardie and Warner 1985; Emanuel and Rotunno 1989; Spengler et al. 2017). Numerical model simulations carried out by Føre et al. (2012) to investigate an intense Arctic PL observed in the Barents Sea during December 2002 suggest that baroclinic instability is important during its initial growth phase, while surface heat fluxes contribute to its mature, convectively-driven phase.

As for classifying different types of PLs, "comma shaped" PLs, associated with weak or moderate surface fluxes, as opposed to "spiral cloud" PLs, characterized by deep convection (Rasmussen and Cederskov 1994; Businger and Reed 1989), have been observed. Claud et al. (2009a) noted

that comma cloud vortices typically represent deep baroclinity occurring within the larger circulation of frontal cyclones whereas spiral cloudform PLs tend to occur within cold air under more barotropic and convective conditions. Terpstra et al. (2016) and Spengler et al. (2017) proposed a unifying moist baroclinic paradigm based on the angle between the thermal wind and mean wind, separating forward shear versus reverse shear environments, the former being characterized by deep baroclinity, and the latter associated with occlusions and shallow low-level baroclinity.

Among other possible mechanisms contributing to PL genesis, convective instability of the second kind (CISK), as for TCs, was considered (Rasmussen 1979, 1985). In addition, barotropic instability associated with horizontal wind shear of the background flow (Rasmussen and Cederskov 1994; Rasmussen et al. 1996; Asai and Miura 1981), has been investigated. The modeling study by Nagata (1993) found that low-level barotropic shear instability was the dominant mechanism for the development of meso-β cyclones along the Japan sea Polar airmass Convergence Zone (JPCZ), and Kawashima and Fujiyoshi (2005) showed that meso-γ-scale polar cyclones off the west coast of Hokkaido Island also extracted energy from a line of low-level horizontal shear. The study of a Mediterranean Sea T-LC by Reale and Atlas (2001) showed that strong horizontal wind shear at the *j*et level coupled with weak vertical wind shear slightly to the north of the jet, supported the growth of a vertically aligned vorticity column through extraction of kinetic energy from the jet via barotropic instability, in concurrence with other contributing factors of elevated surface fluxes and low-level convergence.

b. Polar Lows in global analyses

The representation of polar lows in state-of-the-art global analyses is affected by difficulties comparable to the ones that existed for tropical cyclones in the mid 2000s. At that time, global operational forecasting systems were steadily improving their representation of TCs and track

prediction, however, intensity was vastly underestimated partly due to insufficient horizontal resolution, wherein only signatures of tropical cyclones (such as "warm core eddies interpreted as tropical storms") were used as indication of TC activity in climate models (Bengsston et al. 2007). Currently, operational global analyses (with horizontal resolution of the order of about $10-15\,km$), as well as high-resolution climate models, contain increasingly more realistic depictions of tropical cyclones, but the same cannot yet be said for polar lows. Quite often, PLs (and T-LCs) are either missed or not fully resolved in global analyses and models, and a clear sea-level pressure minimum is not always detected. The analysis of PLs is more challenging than TCs because of: a) their smaller scale, of the order of few hundreds of kilometers, b) rapid development, involving multi-scale processes, c) much shorter lifespan, often of a day or less, d) erratic behavior, e) sparsity of conventional observations in high-latitude oceanic regions, f) poor coverage by geostationary satellites in the high latitudes and, most important, g) *difficulty of objectively validating the analysis.*

In fact, unlike TCs, a global, comprehensive, observation-based "best track" data base for PLs does not yet exist. Although a clear PL detection from infrared or microwave sensors onboard polar orbiting platforms is possible, very often, it is difficult to establish continuity because a PL can drastically change or even disappear between one satellite pass and the next. Moreover, as mentioned above, there is limited coverage of geostationary imagery at high latitudes.

In particular, infrared radiances from the High resolution Infrared Radiation Sounder (HIRS), Advanced Very High Resolution Radiometer (AVHRR), and the MODerate resolution Imaging Spectroradiometer (MODIS) have been used to study the cloud structure associated with PLs (Claud et al. 1993; Blechschmidt 2008; Inoue et al. 2010; Noer et al. 2011; Bobylev et al. 2011; Rojo et al. 2015), whereas microwave radiometer measurements from the Advanced Microwave Sounding Unit (AMSU-A and AMSU-B) and Microwave Humidity Sounder (MHS) have been used to detect brightness temperature signal produced by the warm core and/or cloud properties

associated with PLs (Moore and Vonder Haar 2003; Claud et al. 2009b; Melsheimer et al. 2015). Relevant to our study, the AMSU-B 183 GHz channels are robust in detecting convective PLs due to their sensitivity to the scattering by hydrometeors (Claud et al. 2009b).

However, the above observations are not sufficient to create a global, comprehensive PL data set. Tracking datasets for PLs are limited to northern hemispheric storms (Condron et al. 2006; Xia et al. 2012; Mallet et al. 2013; Zappa et al. 2014; Laffineur et al. 2014; Watanabe et al. 2016; Yanase et al. 2016), with the exception of Verezemskaya et al. (2017) who created a reference dataset for Southern Ocean PLs and mesoscale cyclones.

This paper describes a set of Observing System Experiments (OSEs) focused on improving the analyzed representation of such storms in a global three-dimensional variational (3DVAR) data assimilation system (DAS) through the ingestion of adaptively thinned hyperspectral InfraRed (IR) radiances including over partly cloudy regions. Three cases from the year 2014 are chosen, viz., a northern hemisphere PL, a southern hemisphere PL, and a Mediterranean Sea T-LC. The storms are discriminated as systems forming poleward of the jet stream, following the approach by Ninomiya (1989) and Blechschmidt (2008). For the Southern Ocean PL, results from Verezemskaya et al. (2017) are used as guidance to identify the large-scale environment conducive for its occurrence and growth. Of particular concern for this study is the significance of dynamic instability occurring poleward of the jet in the pre-cyclogenetic environment of PLs and T-LCs.

The article is organized as follows: Section 2 summarizes the progress towards assimilation of cloud-cleared hyperspectral IR radiances, Section 3 describes the model, data assimilation system, and adaptive thinning procedure used in this work, Section 4 provides a brief synoptic background for each storm and the rationale for the experiment set up, Section 5 discusses the results, and Section 6 offers summary and conclusions of this work.

2. Assimilation of cloud-cleared infrared radiances

The cloud-clearing methodology described in Chahine (1974, 1977); Chahine et al. (2006); Susskind et al. (2003); Susskind et al. (2006, 2010), allows to produce IR data in areas that are partly cloudy based on the assumption that cloud formations remain invariant whereas cloud fractions differ within a retrieval Field of Regard (FOR) which consists of multiple Fields of View (FOVs). For each FOR, this assumption allows to estimate cloud effects as proportional to cloud fraction using simple multiple linear equations, without modeling or prior knowledge of cloud optical and spectral properties. $3x3$ FOVs constitute 1 FOR in the case of the Atmospheric InfraRed Sounder (AIRS) onboard NASA Aqua satellite which is the dataset used for assimilating adaptively thinned and cloud-cleared IR radiances in our study.

Early studies comparing the assimilation of AIRS cloud-cleared retrievals with clear-sky radiances, aside from documenting an improvement in global forecast skill (Reale et al. 2008), described a positive impact on the representation of tropical cyclogenetic processes and TCs over the Atlantic Ocean (Wu et al. 2006; Reale et al. 2009b), and on the analysis and forecast of a particularly challenging storm: the infamous TC Nargis (Reale et al. 2009a) which was missed in the operational analyses of the time despite having reached sustained winds in excess of 32 $m\,s^{-1}$. In addition, assimilation of AIRS cloud-cleared retrievals was shown to improve the prediction of extreme precipitation associated with hurricanes (Zhou et al. 2010) and large-scale synoptic forcings (Reale et al. 2012). In spite of the benefits of assimilating IR information derived in the presence of clouds as demonstrated by these studies, it could not be adopted in an operational context: operational centers worldwide had since long opted for radiance assimilation over retrievals, because of better control of errors and latency.

Attempts of assimilating IR radiances affected by clouds have been very encouraging but sporadic. Pangaud et al. (2009) showed that assimilating AIRS radiances affected by mid- to low-level clouds had a positive impact on the development, track, and intensity forecast of a Mediterranean T-LC; Singh et al. (2011) demonstrated improvements in mesoscale predictions over the Indian region; while Wang et al. (2017) explored the impact on Atlantic TCs.

More recently, Reale et al. (2018), while investigating the assimilation of AIRS cloud-cleared radiances (CCRs) and possible obstacles that may have hindered their use, demonstrated that AIRS CCRs must be thinned more aggressively, i.e., assimilated at a much *lower density* globally, compared to clear-sky radiances in order to produce a positive impact. Since AIRS CCRs are obtained by combining 9 FOVs, they are likely to have a broader spatial representativeness and/or higher horizontal error correlation, which in turn requires more aggressive thinning prior to assimilation. Reale et al. (2018) found the best global forecast skill when assimilating AIRS CCRs at roughly $\sim 1/4^{th}$ density of clear-sky. In order to further improve their impact, Reale et al. (2018) proposed a simple adaptive thinning methodology that uses two different thinning levels, which leads to assimilation of AIRS CCRs at a lower density globally, and higher density only around TCs. This approach is consistent with the idea that additional data are beneficial when horizontal gradients are stronger, and that denser AIRS coverage could improve sampling the temperature gradients associated with the TC upper tropospheric outflow. This simple two-density approach for cloud-cleared IR data assimilation was found to be successful in improving the analyzed representation and forecast of TCs, without deteriorating the global skill (Reale et al. 2018).

The assimilation of AIRS CCRs benefits the TC analysis and forecasts because of an improved thermal representation of the upper troposphere occurring at the very edges of the TC: a small but sharp temperature contrast between the TC outflow and the surrounding cloud-free areas, which results in the TC becoming slightly warmer than the surrounding cloud-free environment. The

temperature anomaly propagates to the lower-levels through hydrostatic adjustment and creates a deeper, more accurately placed, and more confined circulation (Reale et al. 2009a). A similar consequence of the assimilation of cloud-cleared AIRS information was noted at the edges of large convective systems (Reale et al. 2009b) and, in the vicinity of broken Arctic stratus clouds, wherein the ingestion of AIRS CCRs allowed adjustments to the representation of lower tropospheric temperatures and midtropospheric geopotential height, which, in turn, was found to be beneficial in improving the forecast of individual midlatitude baroclinic waves (McGrath-Spangler et al. 2021).

The objective of the current work is to show that an adaptive thinning methodology for CCRs, as done for TCs (Reale et al. 2018), can be successfully applied to extratropical mesoscale convective cyclones such as Polar Lows and Mediterranean T-LCs. A set of OSEs is presented, and the analyzed representation of three storms are investigated in each experiment, viz., a PL that developed over the Okhotsk Sea on 10 October 2014, a Southern Ocean Antarctic PL that developed on 23 September 2014, and a Mediterranean Sea T-LC (named "Qendresa") observed on 7 November 2014.

3. Methodology

a. Model and Data Assimilation System

The OSEs discussed in this study were performed using the NASA Goddard Earth Observing System (GEOS) data assimilation and forecast system (version 5.13.0p1), which is developed at the Global Modeling and Assimilation Office (GMAO) and combines a 3DVAR DAS based on the Gridpoint Statistical Interpolation (GSI) analysis scheme (Wu et al. 2002; Kleist et al. 2009b), with a cubed-sphere, hydrostatic global atmospheric model (Molod et al. 2012), run at approximately a quarter degree horizontal resolution with 72 vertical layers. The DAS used in these experiments

is very close to the one adopted for the production of the Modern-Era Retrospective Analysis for Research and Applications, version 2, which is documented by Gelaro et al. (2017) and includes several modifications compared to the earlier GEOS described by Rienecker et al. (2008). The minimization procedure uses a tangent linear mode constraint (Kleist et al. 2009a) whereas the terms in the background error covariance matrix are estimated following the methodology created by Parrish and Derber (1992), i.e., by calculating departures in the 24- and 48- hour forecasts. It should be clarified that the GEOS used in this research is not the current version adopted by the GMAO, which at the time of this article operates a hybrid four-dimensional ensemble variational system (4DEnVAR). The choice of the 3DVAR version was necessary because OSEs must be performed with a frozen system. The control references runs had been already produced with the 3DVAR version (version 5.13.0p1), and any new experiment had to follow the same setup. Furthermore, OSEs are very computationally expensive and to create new control runs was not possible.

b. Experiment setup

The purpose of the OSEs described in this article is to propose a strategy to improve the analyzed representation of three individual storms, each quite representative of its own, selected from the boreal fall period of 2014. The two key points are to demonstrate the usefulness of cloud-cleared radiances, and the importance of adaptively thinning the radiances prior to assimilation.

Two reference experiments, serving as control, are used to assess the impact of the proposed methodology. The first control experiment, named RAD, is run from 1 September to 10 November 2014, assimilating all operationally used observations at that time, including AIRS clear-sky radiances thinned through a $145\,km \times 145\,km$ regular grid. This experiment mimics the operational setup at that time. The second reference experiment, named CLD3, is run for the same time

period but assimilates AIRS CCRs instead of clear-sky radiances, thinned regularly using a grid of $300\,km \times 300\,km$ ($\sim 1/4^{th}$ of the radiances assimilated in RAD, which was found to be the optimal global density for assimilation of CCRs). Both RAD and CLD3 are the same as in Reale et al. (2018), and are also compared in the recent work by McGrath-Spangler et al. (2021).

The experiments named SThinPL, which are the core of this study, result from the design and implementation of an innovative adaptive thinning strategy for AIRS CCRs, targeting three different mesoscale convective cyclones occurring outside the deep tropics. SThinPL uses the same global thinning box as CLD3 except in the vicinity of the storms as described in the following section.

c. Design of adaptive thinning experiments for Polar Lows

The adaptive thinning methodology for TCs described by Reale et al. (2018) requires a TC-centered moving domain, called "TC domain", that follows the TC throughout its lifetime. Within the TC domain, thinning boxes are smaller, which means that radiances are assimilated at a higher density compared to outside the domain. TC center positions can be obtained in real-time from the so-called TC-vitals (Trahan and Sparling 2012). For research purposes, TC center positions in delayed time are obtained from the National Hurricane Center–Joint Typhoon Warning Center TC Best Track database (Knapp et al. 2010). The concept of the TC-centered adaptive thinning methodology is visually illustrated in Reale et al. (2018), their Figure 8. The TC vitals message, cointaining presence and position information, activates a switch in the thinning levels, wherein the thinning boxes become smaller within the moving TC domain. Once the TC is dissipated, if no other TCs are present elsewhere, TC vitals data are no longer received, and thinning again resumes to being globally homogenous. For the GEOS version used by Reale et al. (2018), which is the same version used in this study, the optimal adaptive thinning parameters resulting out of several

experiments were: TC domain size of $15^o \times 15^o$, thinning box of $300\,km \times 300\,km$ globally, and thinning box of $145\,km \times 145\,km$ inside the TC domain.

For the purpose of this work, which is to provide a roadmap to improve operational predictions of Polar Lows and extratropical mesoscale convective cyclones, the major obstacle is that a global real-time standardized message on PL existence/position does not exist, nor any global datasets comparable to TC Best Track.

In lieu of such a dataset for PLs, remote sensing observations, synoptic information, and analyses, have been comprehensively combined for each storm, to detect their presence and to estimate their position and spatial and temporal evolution, with the underlying goal of showcasing a common aspect in the identification and tracking of the storms that could allow for automated activation of PL domains in the future.

Specifically, AMSU-B and MHS brightness temperatures (BT) from the $183.31\,GHz$ channel are used for detecting PLs (following Claud et al. (2009b)), while the corresponding cloud structure is investigated using MODIS true color image which are composites produced from three wavelengths of the visible spectrum (centered at $645\,nm$, $555\,nm$, and $469\,nm$). When the storm position can be localized with the the above-referred satellite data and/or additional synoptic information, the "PL domain" is centered on such positions.

However, because of the short-lasting nature of such systems, information from the model analysis in the time-steps preceding the storm's appearance are also used to identify cyclogenetic dynamical forcings, which in this work, is assumed to occur in the cyclonically sheared portion of the jet stream where maximum horizontal velocity gradients exist. It is worth noting that all three storms investigated in this work occur poleward of the jet stream or one of its meanders, i.e., in the region with potential for maximum cyclonic shear. Within PL domains, AIRS CCRs are assimilated at higher density or, in other words, using smaller thinning boxes ($145\,km \times 145\,km$),

whereas $300\,km \times 300\,km$ thinning boxes (i.e. lower density) are used globally outside the PL domains. A schematic of the methodology is presented in Figure 1 to illustrate the case of a moving PL domain following the jet maximum, and always positioned on its poleward side. The following section provides brief synoptic descriptions, rationale for identification, and the design of the PL domain for each of the three storms.

4. Synoptic discussion, Identification, and Thinning Strategy

a. Polar Low in the Sea of Okhotsk

On 10 October 2014 an intense PL is identified in the Okhotsk Sea (northwestern Pacific) by the Japan Meteorological Agency (JMA). The presence of the storm is confirmed by satellite data: in fact, the Aqua MODIS true color image at 0335 UTC on 10 October 2014 shows a spiral cloud formation over the area (Figure2(a)). A minimum in AMSU-B/MHS brightness temperatures (0156 to 0350 UTC on 10 October; Figure 2(b)) is located around 143° E and 46° N, off the southern coast of Sakhalin, indicating convective cloud top associated with the spiral cloud. It is surrounded by higher brightness temperature values indicating clear regions of subsidence between the spiral bands. Based on satellite information, this appears to be an example of an intense convective polar low. The 0600 UTC surface weather chart analysis produced by the JMA (Figure 2(c)), confirms a polar low at this location, with a central pressure of $992\,hPa$.

Ninomiya (1989) found that PLs occur frequently during October to April in the Okhotsk sea, often developing in the vicinity of a midtropospheric cutoff low or a mesoscale vortex embedded within a synoptic scale trough, to the west-southwest of the main synoptic low that is typically located over the Aleutian Islands. In the RAD analysis at 06z 10 October 2014 (Figure 3), an occluded synoptic cyclone is evident just west of the Aleutian Islands, and a baroclinically active

surface low is evident to its W-SW (off the southern coast of Sakhalin) matching in geographical location with the observed PL (Figure 2(c)). This surface low occurs to the southeast of the mid-tropospheric synoptic scale trough situated along the Siberian coastline, and is vertically aligned with an upper-level mesoscale vortex embedded within the synoptic trough (Figure 3), in remarkable consistency with the PL genesis mechanism described by Ninomiya (1989).

This mesoscale instability, in fact, appears to originate in the upstream flow over Central Asia to the east of the Altai mountain range between 00z to 12z 08 October 2014 as shown in the vorticity field of RAD analysis (Figure 4), associated with strong horizontal velocity gradients of the jet streak. White et al. (2017) found that the orography of Mongolian mountains is an important influence on the upper-level jet and Pacific wintertime atmospheric circulation. The downstream positive vorticity anomaly caused by lee cyclogenesis depends on the horizontal wind speed of the jet. The top panel of Figure 4, shows upper-level wind speeds of the order of $60\,ms^{-1}$ directly above the mountain range and to the west of a shallow mesoscale vortex. Strong horizontal velocity gradients can be noted on the cyclonically sheared side of the jet, while vertical shear poleward of the jet is virtually zero, which suggests the possibility of barotropic instability at the jet level. As the jet propagates eastward and downstream of the mountain, its core (region of maximum winds) splits into two, yielding separate jet streaks (bottom panel of Figure 4). The shallow mesoscale vortex simultaneously expands into the upper troposphere (center and bottom panels of Figure 4) likely aided by upper-level divergence (rising motion) that is known to occur to the poleward side of the exit region of the jet streak.

The $250\,hPa$ streamlines show a meander developing in the jet stream around 18z 08 October (Figure 5). A surface low forms along the eastern side of the meander at 06z 09 October (Figure 5), likely aided by upper-level potential vorticity advection, yielding a baroclinically unstable environment conducive for frontogenesis. The strongest horizontal temperature gradients are

confined to the lower troposphere (not shown) resulting in a sub-synoptic mesoscale front. Cold air advection occurs to the west-northwest of the surface low, and it undergoes rapid frontogenesis occluding in just 18 hours, leading to a favorable environment for PL genesis off the coast of Sakhalin Island. Figure 6 shows the occluded mesoscale front, and the incipient polar low at 00z 10 Oct 2014. Although the PL is relatively shallow at this time, it is accompanied by low-level wind speed maxima of the order of 24 ms^{-1}, as well as the development of a warm core which is indicative of convective heating fueled by upward sensible and latent heat fluxes from the ocean to the cold continental air mass.

For the SThinPL experiment that assimilates variable density AIRS CCRs, a PL domain of size 8° latitude by 10° longitude surrounding and following the mesoscale vortex (shown in Figure 4) is designed. For the times preceding the formation of the storm, the northern edge of the jet streak, which as noted is strongly cyclonically sheared, is assumed to play a key role in the cyclogenetic process, and the PL domain is designed to follow the potentially unstable area starting from 00z 08 October (Figure 5). The enhanced density assimilation within the PL domain is performed until 12z 10 October as shown in Figure 5.

b. Polar Low in the Southern Ocean

The detection and tracking of Antarctic PLs carry the additional challenge of fewer observations over the Southern Ocean, necessitating the use of analyses, in addition to satellite data, for identifying the large-scale environment that could be conducive for occurrence of these storms (Verezemskaya et al. 2017). In this article, an Antarctic PL developing on 23 September 2014 is identified with the aid of Aqua MODIS and AMSU-B/MHS brightness temperatures. Figure 7 shows the Aqua MODIS true color image at 0720 UTC and the AMSU-B/MHS brightness temperatures (between 0707 – 0854 UTC) on 23 September 2014 over the Southern Ocean. The MODIS

image reveals a "comma shaped" cloud occurring within a post-frontal occlusion zone off the coast of East Antarctica, in a region previously confirmed to have maximum PL frequency (Verezemskaya et al. 2017). To the east of this feature, the cloud field associated with an occluded front is clearly evident (left panel of Figure 7). The characteristic hook shape that is commonly associated with a comma cloud PL is visible in the AMSU-B/MHS brightness temperatures (around 57° S and 111° E; right panel of Figure 7) with lower values indicative of higher convective cloud top.

In the RAD analysis (Figure 8), a large-scale occluded cyclonic circulation, encompassing multiple minima, is situated along the sea ice margin at 06z on 21 September 2014 extending from 50° E to 140° E. Evidence of an occluded front (shown in purple in Fig. 8), associated with one such minima (indicated as 'L' in Fig. 8) is presented. Cold, dry Antarctic air was first advected over the sea ice and then over the ice-free ocean in this situation. This low-pressure cold occlusion environment is most favorable for PL development (Verezemskaya et al. 2017). In the RAD analysis, multiple short-lived shallow vortices develop at the edge of the occluded front shown in Fig. 8. In particular, one of these grows into a spurious PL that reaches maximum intensity at 12z 22 September 2014 (Fig. 9) but is not verified by AMSU-B/MHS satellite observations (Fig. 10). A second PL, rapidly develops at the northeast edge of the occluded cyclone, where strong upper-level horizontal wind shear occurs on the poleward side of the jet, and reaches maximum intensity at around 12z 23 September in the RAD analysis. This system is verified in corresponding satellite observations (Figure 7). Once again, the presence of horizontal velocity gradients at the jet level appears to be a crucial dynamical forcing contributing to cyclogenetic processes for this type of systems.

The production of a spurious low in the analysis indicates that the model responds to a favorable environment, however, it does not have enough information to constrain the available energy.

The underlying working idea is that additional AIRS cloud-cleared radiances in this dynamically sensitive environment can improve the analysis.

In this case, as the slow-moving large-scale dynamics of the occluded cyclone are favorable for the development of PLs, the PL domain for SThinPL experiment is designed to assimilate enhanced density AIRS CCRs in a larger, relatively stationary region which encapsulates the polar jet and the area to its south (ranging between 65° S to 45° S). The domain extends from 80° E to 110° E for the period beginning 00z 18 September to 00z 23 September, and covers 100° E to 130° E for the period beginning 06z 23 September to 06z 25 September. Figure 11 shows the domain boundaries for the two periods at snapshots corresponding to the hour of maximum intensity of the two lows (spurious and observed PL) in the RAD analysis.

c. Tropical-like Cyclone"Qendresa"

T-LC "Qendresa" developed in the central Mediterranean Sea to the west of Malta at 12z 07 November 2014. For this storm, Pytharoulis (2018) created a best track dataset starting from 12z 07 November to 06z 08 November 2014, using 3-hour infrared imagery from the Meteosat geostationary satellite, operated by the European Organization for the Exploitation of Meteorological Satellites (EUMETSAT). The study further used 6-hour European Center for Medium-range Weather Forecasts (ECMWF) operational analysis to track the storm prior to its tropical transition (from 00z - 06z 07 November) and post its extratropical transition (from 12z 08 - 00z 09 November), respectively. Therefore, the design of the SThinPL experiment focused on Qendresa is simpler, with the previously published best track data by (Pytharoulis 2018) being used to construct the PL domain.

Pytharoulis (2018) attributed the formation of Qendresa to low-level baroclinic instability coupled with upper-level synoptic forcing, and noted that a sea level pressure of $\sim 984\,hPa$ was recorded at

around 1634 UTC when the storm made its first landfall at Malta. Following landfall at Malta, the T-LC continued to propagate in the east-northeast direction until 21z 07 November, then moving northward and recurving back towards Sicily to make its second landfall along its eastern coast at around 06z 08 November, as a weaker system but causing damages in the Catania area of east Sicily.

Figure 12(a) shows a mesoscale surface low in the RAD analysis along the edge of a warm front off the coast of Tunisia in the Gulf of Gabe at 00z 05th November 2014. Widespread deep convection was observed in the satellite imagery in the central Mediterranean Sea region from the Tyrrhenian basin to the region between Sicily and Africa on 6th November 2014 which is confirmed by local maxima in observed lightning activity (Pytharoulis 2018). A meridionally elongated cold front extending from south of Tunisia to the west of Sicily is observed at 06z 06th November 2014 in the RAD analysis (Fig. 12(b)), in agreement with the ECMWF analysis (Pytharoulis 2018). In both RAD and ECMWF analyses, the T-LC originates within this pre-existing frontal low-pressure environment. As the parent low finally occludes in the central Mediterranean Sea region to the west of Malta, it transitions into a tropical storm at 12z 07th November in the RAD analysis (Fig. 12(c)). This is the hour where tropical storm characteristics, such as a spiral cloud structure and cloud-free eye, were first observed in infrared satellite imagery, marking the genesis of the T-LC (Pytharoulis 2018). As there is excellent agreement of storm genesis conditions in RAD analysis with that observed in ECWMF analysis and satellite data, it is reasonable to construct a moving adaptive thinning domain using the best track dataset created by Pytharoulis (2018).

For the SThinPL experiment, increased density AIRS CCRs are first assimilated within a stationary PL domain of size 4 ° latitude x 5 ° longitude starting from 00z 05th November to 18z 06th November 2014, in the region to the north of Africa and south of Sicily where a prolonged surface depression exists (as shown in Figures 12(a) and (b)). The experiment then uses the same

sized moving PL domain for variable density assimilation changing only the central location of the domain every 6 hours based on the best track obtained from Pytharoulis (2018).

It is very important to note that while information comparable to a best track dataset is used here, this storm also forms to the poleward side of the northern hemisphere subtropical jet, further corroborating the idea that the dynamical forcing associated with the cyclonically sheared side of an upper tropospheric jet could play an important role in the development of extratropical mesoscale convective cyclones, and should be explored as a feature used to automate the activation of PL domains in future modeling studies when real-time track information is not available.

In the following section, the storm structure, evolution, and intensity are investigated in the SThinPL experiment, and compared to the two reference experiments (RAD and CLD3). For Qendresa, as the best track (based on infrared satellite imagery) is available at 3-hourly interval, it is prudent to compare the assimilated instead of analyzed model fields from each experiment which are available at a similar higher temporal resolution as best track observations. Both assimilated and analyzed fields largely represent a blend between the GEOS model and observations, and can be used interchangably for the purpose of our study.

5. Results and Discussion

a. Sea of Okhotsk Polar Low

The Okhotsk Sea PL develops in the environment of an occluded mesoscale front (Figure 6). The upper tropospheric flow, characterized by a jet stream with very strong horizontal velocity gradients, is a likely dynamical contributor to the cyclogenetic process, as noted in section 4(a). A shallow vortex forms on the cyclonically sheared side of the jet (Figure 4), and propagates along with the westerly flow into the ocean (Figure 5), where it transforms into a PL at 00z 10

October 2014 (Figure 6). The storm in all three analyses has higher central pressure compared to JMA observations, with SThinPL analysis having slightly lower value (better representation) compared to the two reference analyses. However, as noted previously, probably because of inadequate resolution, sea level pressure is not a good indicator of PL intensity in global analyses. Condron et al. (2006) advocated the use of vorticity maxima instead of sea level pressure minima to investigate polar mesoscale cyclones in global reanalyses. In this paper, we use *vertically integrated vorticity* to assess and compare the storm's intensity between the three analyses. The maximum vertically integrated vorticity (surface to 300 hPa) at the time of its first detection (00z 10 October 2014) is comparable for all three analyses. The PL continues to propagate eastward, reaching peak intensity at 12z 10 October, followed by rapid dissipation. The SThinPL analyses has stronger intensification of the storm compared to RAD and CLD3 cases.

Figure 13 compares the storm characteristics at 12z 10 October. The storm in the SThinPL analysis shows better alignment between the surface low and upper level vortex, a more compact warm core, stronger low-level winds, deeper and more symmetric vertical structure compared to RAD (Figure 13). The vertically integrated vorticity associated with the PL at peak intensity, which represents the "signature" of the storm, is substantially higher in SThinPL analysis (around 30% and 50% more than RAD and CLD3, respectively). The strong impact obtained on the storm's vorticity signature, wind speed, vertical extent, alignment and compactness of the warm core suggests that the assimilation of higher density cloud-cleared radiances in the pre-cyclogenetic stages, within a domain centered on high horizontal velocity gradients located on the poleward edge of a jet streak, may be a successful strategy and could lead to even better results with higher model resolution.

b. Southern Ocean Polar Low

The Southern Ocean PL forms in a post-occlusion baroclinic environment as noted in section 4(b). In Figure 14, a vorticity maximum forms at about 110^oE at 00z 23 September in all three analyses. As noted previously in section 4(b), there is also a spurious low in all analyses at this time, occurring to the west of the vorticity maximum described above, which is not verified in the observations and disappears in the following time step.

The wind structure illustrated in the meridional cross-section (bottom panel of Fig. 14) reveals a strong upper level jet, with core at about or slightly north of 50^oS, and very sharp horizontal velocity gradients between 1000 hPa and 400 hPa, with almost vertical isotachs, occurring poleward of the jet core at about 55^oS. This is the location where the mesoscale vortex develops, indicating the plausibility of cyclonic vorticity production from barotropic energy conversion. Such gradients are substantially stronger in the SThinPL case, supporting the development of a stronger mesoscale vortex which is evidently shredded above 600 hPa because of vertical wind shear (right panel of Fig. 14). As the vertical wind shear relaxes in the upper levels, the vortex subsequently develops into a PL reaching maximum intensity at 12z 23 September 2014 (right panel of Fig. 15) and rapidly dissipating after. The occurrence of the PL at this location is confirmed using satellite observations (Fig. 7). The 10m winds observed around this time by the Advanced Scatterometer (ASCAT) instrument onboard the EUMETSAT Metop-b satellite, confirm a tighter low-level cyclonic circulation surrounding the PL as compared to model analyses (not shown). At peak intensity, the storm in SThinPL experiment benefits from more vigorous upper-level forcing compared to RAD, as indicated by lower 500mb geopotential height values (top panel of Fig. 15) and enhanced vorticity in upper and lower levels (bottom panel of Fig. 15).

As a consequence, the PL in SThinPL analysis is deeper, with a more pronounced warm core, stronger vertically integrated vorticity, and better vertical alignment (Fig. 15). Figure 14 suggests that, similar to the northern hemisphere PL, the dynamical instability occurring at the poleward edge of the jet stream can be crucial for cyclogenetic processes associated with the Southern Ocean PL, and enhanced CCR assimilation in this region could lead to improved analyzed representation of the storm (Fig. 15).

c. Tropical-like Cyclone Qendresa

As discussed in section 4(c), satellite observations and model analyses confirm that T-LC Qendresa developed in the central Mediterranean Sea to the west of Malta at 12z 07 November 2014, and subsequently made two landfalls: first at Malta, and the second along the eastern coast of Sicily. Following the first landfall, the storm undergoes extratropical transition in all three analyses.

Figure 16 compares the T-LC's characteristics in the SThinPL case against RAD and CLD3 analyses at 15z 07 November, which is the time-step right before the first landfall. The storm occurs at the poleward edge of the subtropical jet stream, in a region characterized by relatively weak vertical wind shear in the lower levels, coupled with relatively high horizontal winds to the south and west of the storm. The storm exhibits tropical characteristics including a warm core in all three analyses.

Overall, the storm in SThinPL is much more compact (compare center panel of Fig. 16), with stronger low-level vorticity, and a more pronounced warm core. Moreover, compared to the other two analyses, the SThinPL case has the maximum vertically integrated vorticity at this time, which represents the true signature of the system in the analysis. The center pressure reaches $\sim 996\, hPa$ in SThinPL and is slightly deeper compared to RAD and CLD3, however, it is higher than the station observation (see discussion in section 4(c)). As noted before, sea level pressure is likely to

be underestimated for such small-scale storms due to the limiting horizontal resolution adopted for this work.

6. Summary and Concluding Remarks

This study is an expansion of previous work by Reale et al. (2018) who demonstrated a positive impact on the representation of Tropical Cyclones through the assimilation of *adaptively thinned cloud-cleared IR radiances* (as opposed to homogenously thinned clear-sky radiances) in a global modeling and data assimilation system. Here, a similar methodology is applied to Polar Lows and Tropical-like Cyclones, focusing on three storms, viz., a northern hemisphere PL, an Antarctic PL, and a Mediterranean Sea T-LC that occurred during the 2014 boreal fall period.

The adaptive thinning methodology proposed by Reale et al. (2018) uses a homogenous thinning box for assimilating hyperspectral IR radiances globally except when TCs are present. In the presence of TCs, IR radiances are thinned less aggressively, with smaller thinning boxes (i.e. more radiances being assimilated) inside a moving domain centered on the TC. A trigger, containing information on TC existence and position as provided by the TC-vitals (in real-time) or Best Track information (for hindcasting experiments), is needed to activate and de-activate the adaptive procedure. The activation of the trigger is performed from the time in which a storm is detected at its earliest stage (i.e., tropical depression) until it ceases to exist or transitions to an extratropical system.

The challenge faced in this work is that information comparable to TC-vitals does not exist for Polar Lows on a global scale. Furthermore, even when PLs can be identified from satellite imagery or other observations, their development and dissipation can be extremely short-lived (sometimes lasting for only 12 hours), therefore limiting the duration, and most likely, the effectiveness of the adaptive procedure. In an attempt to obviate these limitations, a comprehensive assortment of

synoptic, model, and satellite information are reviewed and used to identify and track the instability associated with these storms. While the review process and background for the three storms are significantly different, this work identifies one common aspect between them: all three storms form on the poleward side of a subtropical or polar jet. Specifically, it is shown that strong local wind speed maxima traveling within the jet precedes the formation of each system. In order to allow enhanced density IR radiance assimilation, activation of a moving "PL domain" positioned on the area poleward of this speed maxima in the hours preceding the formation of the storm, and thereafter following the storm, is plausible, and allows for an improved representation of the storm in the model analysis.

The analyses obtained with the adaptive procedure described in this study for each storm are compared against the analyses produced by assimilation of homogenuously thinned AIRS clear-sky radiances and homogeneous thinned AIRS cloud-cleared radiances. For each storm, a positive impact on intensity and storm structure is noted (specifically, on vertically integrated relative vorticity maxima, warm core strength, depth, symmetry, vertical alignment, and compactness). All these results are in agreement with the findings by Reale et al. (2018), suggesting that enhancing the representation of temperature gradients between the cloud top edges and the surrounding environment (which is a direct consequence of assimilation of CCRs) leads to better analyzed storms. Even though the adaptive thinning methodology adopted in this study has demonstrated a positive impact on the analyzed representation of PLs in the NASA GEOS system, it should be clarified that an accurate representation of PL intensity and structure continues to remain challenging for global analyses and models due to their small size, dominance of convective processes, explosive development in poorly observed oceanic regions, and difficulty in objectively validating them in analysis.

In summary, this study indicates a possible pathway for an automated adaptive thinning methodology for IR radiances centered on local wind speed maxima at the jet level, as defined by the background or immediately preceding analyses, in order to better represent marine extratropical mesoscale convective cyclones. The rationale for such an approach is supported by decades of work indicating PLs preferred formation on the poleward edge of a polar jet stream in a region with strong horizontal wind speed gradients (Reed 1979; Ninomiya 1989; Rasmussen and Turner 2003; Blechschmidt 2008). Reale and Atlas (2001) suggested that jet-level barotropic instability could be a contributing factor to small-scale convective cyclones in the extra tropics, in the presence of extremely high horizontal wind shear that is large enough to overcome the Coriolis parameter at the given latitude.

Some caveats associated with this work are: the limited number of case studies, the use of a 3DVAR framework, and the focus on a single hyperspectral IR sensor (viz. AIRS). However, the methodology is being tested in the hybrid 4DEnVAR assimilation system currently adopted by the operational GEOS with promising results. Futhermore, preliminary successful results (not shown in this work) with the Cross-track Infrared Sounder (CrIS) on board NOAA satellites suggest that the cloud-clearing methodology and TC-based adaptive thinning approach are applicable to other infrared sensors producing comparable or better results. Assimilation of IR radiances from the Infrared Atmospheric Sounding Interferometer (IASI) onboard European polar-orbiting MetOp meteorological satellites has already shown a positive impact on the forecast of Arctic PLs even when assimilating clear-sky radiances (e.g., the regional modeling study by Randriamampianina et al. (2011)). The implementation of adaptive methodologies and the improved use of IR radiances in areas affected by clouds, as suggested by this study, may prove beneficial also to the current IASI and future IR sensors.

Acknowledgments. The authors gratefully acknowledge support from Dr. Tsengdar Lee (NASA HQ) through NASA grant 80NSSC18K0927 and for allocations on NASA High-End Computing resources. The authors also acknowledge Dr. Will McCarty and Dr. Ronald Gelaro for valuable scientific advice, the Global Modeling and Assimilation Office for the use and development of the GEOS, and Dr. Chris Barnet for his leadership on the development of cloud-cleared radiance algorithms. All simulations were performed at the NASA Center for Climate Studies (NCCS) in Greenbelt, Maryland. AIRS data are distributed by the NASA Distributed Active Archive Center (DAAC) Goddard Earth Sciences Data and Information Services Center (GES DISC).

Data availability statement. The numerical model simulations upon which this study is based are too large to archive or to transfer. Instead, we provide all the information needed to replicate the simulations; we used the NASA Goddard Earth Observing System (GEOS) model and 3DVAR data assimilation system (version 5.13.0p1). The GEOS source code is available under the NASA Open-Source Agreement at http://opensource.gsfc.nasa.gov/projects/GEOS-5. The AIRS CCRs can be downloaded at https://disc.gsfc.nasa.gov/. MODIS true color images can be obtained at https://neo.sci.gsfc.nasa.gov/. The AMSU-B and MHS Brightness Temperature data are available at https://www.ncei.noaa.gov/. The JMA Surface Weather Chart can be obtained from the Japan Meteorological Agency website at https://www.data.jma.go.jp/fcd/yoho/wxchart/

References

Almazroui, M., A. M. Awad, and M. N. Islam, 2018: Characteristics of the internal and external sources of the Mediterranean synoptic cyclones for the period 1956–2013. *Theoretical and Applied Climatology*, **133 (3-4)**, 811–827, doi:10.1007/s00704-017-2218-2, URL https://doi.org/10.1007/s00704-017-2218-2.

Asai, T., and Y. Miura, 1981: An Analytical Study of Meso-Scale Vortex-Like Disturbances Observed around Wakasa Bay Area. *Journal of the Meteorological Society of Japan. Ser. II*, **59 (6)**, 832–843, doi:10.2151/jmsj1965.59.6_832, URL https://doi.org/10.2151/jmsj1965.59.6_832.

Blechschmidt, A.-M., 2008: A 2-year climatology of Polar Low events over the Nordic Seas from satellite remote sensing. *Geophysical Research Letters*, **35 (9)**, doi:10.1029/2008GL033706, URL https://agupubs.onlinelibrary.wiley.com/doi/abs/10.1029/2008GL033706.

Bobylev, L. P., E. V. Zabolotskikh, L. M. Mitnik, and M. L. Mitnik, 2011: Arctic Polar Low Detection and Monitoring Using Atmospheric Water Vapor Retrievals from Satellite Passive Microwave Data. *IEEE Transactions on Geoscience and Remote Sensing*, **49 (9)**, 3302–3310, doi:10.1109/TGRS.2011.2143720, URL https://doi.org/10.1109/TGRS.2011.2143720.

Businger, S., and R. J. Reed, 1989: Cyclogenesis in Cold Air Masses. *Weather and Forecasting*, **4 (2)**, 133–156, doi:10.1175/1520-0434(1989)004<0133:CICAM>2.0.CO;2, URL https://doi.org/10.1175/1520-0434(1989)004<0133:CICAM>2.0.CO;2.

Chahine, M. T., 1974: Remote Sounding of Cloudy Atmospheres. I. The Single Cloud Layer. *Journal of the Atmospheric Sciences*, **31 (1)**, 233–243, doi:10.1175/1520-0469(1974)031<0233:

RSOCAI>2.0.CO;2, URL https://doi.org/10.1175/1520-0469(1974)031<0233:RSOCAI>2.0.CO;2.

Chahine, M. T., 1977: Remote Sounding of Cloudy Atmospheres. II. Multiple Cloud Formations. *Journal of the Atmospheric Sciences*, **34 (5)**, 744–757, doi:10.1175/1520-0469(1977)034<0744:RSOCAI>2.0.CO;2, URL https://doi.org/10.1175/1520-0469(1977)034<0744:RSOCAI>2.0.CO;2.

Chahine, M. T., and Coauthors, 2006: AIRS Improving Weather Forecasting and Providing New Data on Greenhouse Gases. *Bulletin of the American Meteorological Society*, **87 (7)**, 911–926, doi:10.1175/BAMS-87-7-911, URL https://doi.org/10.1175/BAMS-87-7-911.

Claud, C., A. M. Carleton, B. Duchiron, and P. Terray, 2009a: Southern hemisphere winter cold-air mesocyclones: climatic environments and associations with teleconnections. *Climate Dynamics*, **33 (2-3)**, 383–408, doi:DOI:10.1007/s00382-008-0468-5, URL https://doi.org/10.1007/s00382-008-0468-5.

Claud, C., B. Funatsu, G. Noer, and J.-P. Chaboureau, 2009b: Observation of polar lows by the Advanced Microwave Sounding Unit: potential and limitations. *Tellus A: Dynamic Meteorology and Oceanography*, **61 (2)**, 264–277, doi:10.1111/j.1600-0870.2008.00384.x, URL https://doi.org/10.1111/j.1600-0870.2008.00384.x.

Claud, C., N. M. Mognard, K. B. Katsaros, A. Chedin, and N. A. Scott, 1993: Satellite observations of a polar low over the Norwegian Sea by special sensor microwave imager, Geosat, and TIROS-N operational vertical sounder. *Journal of Geophysical Research: Oceans*, **98 (C8)**, 14 487–14 506, doi:10.1029/93JC00650, URL https://agupubs.onlinelibrary.wiley.com/doi/abs/10.1029/93JC00650.

Condron, A., G. R. Bigg, and I. A. Renfrew, 2006: Polar Mesoscale Cyclones in the Northeast Atlantic: Comparing Climatologies from ERA-40 and Satellite Imagery. *Monthly Weather Review*, **134 (5)**, 1518–1533, doi:10.1175/MWR3136.1, URL https://doi.org/10.1175/MWR3136.1.

Emanuel, K. A., and R. Rotunno, 1989: Polar lows as arctic hurricanes. *Tellus A: Dynamic Meteorology and Oceanography*, **41 (1)**, 1–17, doi:10.3402/tellusa.v41i1.11817, URL https://doi.org/10.3402/tellusa.v41i1.11817.

Føre, I., J. E. Kristjánsson, E. W. Kolstad, T. J. Bracegirdle, Ø. Saetra, and B. Røsting, 2012: A 'hurricane-like' polar low fuelled by sensible heat flux: high-resolution numerical simulations. *Quarterly Journal of the Royal Meteorological Society*, **138 (666)**, 1308–1324, doi:10.1002/qj.1876, URL https://rmets.onlinelibrary.wiley.com/doi/abs/10.1002/qj.1876.

Gelaro, R., and Coauthors, 2017: The modern-era retrospective analysis for research and applications, version 2 (merra-2). *Journal of climate*, **30 (14)**, 5419–5454.

Harrold, T. W., and K. A. Browning, 1969: The polar low as a baroclinic disturbance. *Quarterly Journal of the Royal Meteorological Society*, **95 (406)**, 710–723, doi:10.1002/qj.49709540605, URL https://rmets.onlinelibrary.wiley.com/doi/abs/10.1002/qj.49709540605.

Hart, R. E., 2003: A Cyclone Phase Space Derived from Thermal Wind and Thermal Asymmetry. *Monthly Weather Review*, **131 (4)**, 585–616, doi:10.1175/1520-0493(2003)131<0585:ACPSDF>2.0.CO;2, URL https://doi.org/10.1175/1520-0493(2003)131<0585:ACPSDF>2.0.CO;2.

Inoue, J., M. E. Hori, Y. Tachibana, and T. Kikuchi, 2010: A polar low embedded in a blocking high over the pacific arctic. *Geophysical research letters*, **37 (14)**.

Kawashima, M., and Y. Fujiyoshi, 2005: Shear Instability Wave along a Snowband: Instability Structure, Evolution, and Energetics Derived from Dual-Doppler Radar Data. *Journal of the Atmospheric Sciences*, **62 (2)**, 351–370, doi:10.1175/JAS-3392.1, URL https://doi.org/10.1175/JAS-3392.1.

Kleist, D. T., D. F. Parrish, J. C. Derber, R. Treadon, R. M. Errico, and R. Yang, 2009a: Improving incremental balance in the gsi 3dvar analysis system. *Monthly Weather Review*, **137 (3)**, 1046–1060.

Kleist, D. T., D. F. Parrish, J. C. Derber, R. Treadon, W.-S. Wu, and S. Lord, 2009b: Introduction of the gsi into the ncep global data assimilation system. *Weather and Forecasting*, **24 (6)**, 1691–1705.

Knapp, K. R., M. C. Kruk, D. H. Levinson, H. J. Diamond, and C. J. Neumann, 2010: The International Best Track Archive for Climate Stewardship (IBTrACS): Unifying Tropical Cyclone Data. *Bulletin of the American Meteorological Society*, **91 (3)**, 363–376, doi:10.1175/2009BAMS2755.1, URL https://doi.org/10.1175/2009BAMS2755.1.

Laffineur, T., C. Claud, J.-P. Chaboureau, and G. Noer, 2014: Polar Lows over the Nordic Seas: Improved Representation in ERA-Interim Compared to ERA-40 and the Impact on Downscaled Simulations. *Monthly Weather Review*, **142 (6)**, 2271–2289, doi:10.1175/MWR-D-13-00171.1, URL https://doi.org/10.1175/MWR-D-13-00171.1.

Mallet, P.-E., C. Claud, C. Cassou, G. Noer, and K. Kodera, 2013: Polar lows over the Nordic and Labrador Seas: Synoptic circulation patterns and associations with North Atlantic-Europe wintertime weather regimes. *Journal of Geophysical Research: Atmospheres*, **118 (6)**, 2455–2472, doi:10.1002/jgrd.50246, URL https://agupubs.onlinelibrary.wiley.com/doi/abs/10.1002/jgrd.50246.

Mazza, E., U. Ulbrich, and R. Klein, 2017: The Tropical Transition of the October 1996 Medicane in the Western Mediterranean Sea: A Warm Seclusion Event. *Monthly Weather Review*, **145 (7)**, 2575–2595, doi:10.1175/MWR-D-16-0474.1, URL https://doi.org/10.1175/MWR-D-16-0474.1.

McGrath-Spangler, E. L., M. Ganeshan, O. Reale, N. Boukachaba, W. McCarty, and R. Gelaro, 2021: Sensitivity of low-tropospheric arctic temperatures to assimilation of airs cloud-cleared radiances: Impact on midlatitude waves. *Quarterly Journal of the Royal Meteorological Society*, **147 (741)**, 4032–4047, doi:https://doi.org/10.1002/qj.4166, URL https://rmets.onlinelibrary.wiley.com/doi/abs/10.1002/qj.4166, https://rmets.onlinelibrary.wiley.com/doi/pdf/10.1002/qj.4166.

Melsheimer, C., T. Frost, and G. Heygster, 2015: Detectability of Polar Mesocyclones and Polar Lows in Data From Space-Borne Microwave Humidity Sounders. *IEEE Journal of Selected Topics in Applied Earth Observations and Remote Sensing*, **9**, 1–10, doi:10.1109/JSTARS.2015.2499083, URL https://doi.org/10.1109/JSTARS.2015.2499083.

Miglietta, M., D. Cerrai, S. Laviola, E. Cattani, and V. Levizzani, 2017: Potential vorticity patterns in Mediterranean "hurricanes". *Geophysical Research Letters*, **44 (5)**, 2537–2545, doi:10.1002/2017GL072670, URL https://doi.org/10.1002/2017GL072670.

Miglietta, M. M., and R. Rotunno, 2019: Development mechanisms for Mediterranean tropical-like cyclones (medicanes). *Quarterly Journal of the Royal Meteorological Society*, **145 (721)**, 1444–1460, doi:10.1002/qj.3503, URL https://doi.org/10.1002/qj.3503.

Molod, A., L. Takacs, M. Suarez, J. Bacmeister, I.-S. Song, A. Eichmann, and Y. Chang, 2012: The GEOS-5 Atmospheric General Circulation Model: Mean Climate and Development from

MERRA to Fortuna. *NASA Technical Report Series on Global Modeling and Data Assimilation, NASA/TM-2008-104606*, **28**, 115, URL http://gmao.gsfc.nasa.gov/pubs/docs/tm28.pdf.

Moore, R. W., and T. H. Vonder Haar, 2003: Diagnosis of a Polar Low Warm Core Utilizing the Advanced Microwave Sounding Unit. *Weather and Forecasting*, **18 (5)**, 700–711, doi:10.1175/1520-0434(2003)018<0700:DOAPLW>2.0.CO;2, URL https://doi.org/10.1175/1520-0434(2003)018<0700:DOAPLW>2.0.CO;2.

Nagata, M., 1993: Meso-β-scale Vortices Developing along the Japan-Sea Polar-Airmass Convergence Zone (JPCZ) Cloud Band : Numerical Simulation. *Journal of the Meteorological Society of Japan. Ser. II*, **71 (1)**, 43–57, doi:10.2151/jmsj1965.71.1_43, URL https://doi.org/10.2151/jmsj1965.71.1_43.

Ninomiya, K., 1989: Polar/Comma-Cloud Lows over the Japan Sea and the Northwestern Pacific in Winter. *Journal of the Meteorological Society of Japan. Ser. II*, **67 (1)**, 83–97, doi:10.2151/jmsj1965.67.1_83, URL https://doi.org/10.2151/jmsj1965.67.1_83.

Noer, G., and M. Ovhed, 2003: Forecasting of polar lows in the Norwegian and the Barents Sea. *Proc. of the 9th meeting of the EGS Polar Lows Working Group, Cambridge, UK*.

Noer, G., Ø. Saetra, T. Lien, and Y. Gusdal, 2011: A climatological study of polar lows in the Nordic Seas. *Quarterly Journal of the Royal Meteorological Society*, **137 (660)**, 1762–1772, doi:10.1002/qj.846, URL https://rmets.onlinelibrary.wiley.com/doi/abs/10.1002/qj.846.

Pangaud, T., N. Fourrie, V. Guidard, M. Dahoui, and F. Rabier, 2009: Assimilation of AIRS radiances affected by mid-to low-level clouds. *Monthly Weather Review*, **137 (12)**, 4276–4292, doi:10.1175/2009MWR3020.1, URL https://doi.org/10.1175/2009MWR3020.1.

729 Parker, N., and E. Hudson, 1991: *Polar Low Handbook for Canadian Meteorologists*. Atmospheric
730 Environment Service.

731 Parrish, D. F., and J. C. Derber, 1992: The national meteorological center's spectral statistical-
732 interpolation analysis system. *Monthly Weather Review*, **120 (8)**, 1747–1763.

733 Pytharoulis, I., 2018: Analysis of a Mediterranean tropical-like cyclone and its sensitivity to the
734 sea surface temperatures. *Atmospheric Research*, **208**, 167 – 179, doi:10.1016/j.atmosres.2017.
735 08.009, URL https://doi.org/10.1016/j.atmosres.2017.08.009.

736 Randriamampianina, R., T. Iversen, and A. Storto, 2011: Exploring the assimilation of IASI
737 radiances in forecasting polar lows. *Quarterly Journal of the Royal Meteorological Society*,
738 **137 (660)**, 1700–1715, doi:10.1002/qj.838, URL https://rmets.onlinelibrary.wiley.com/doi/abs/
739 10.1002/qj.838.

740 Rasmussen, E., 1979: The polar low as an extratropical CISK disturbance. *Quarterly Journal*
741 *of the Royal Meteorological Society*, **105 (445)**, 531–549, doi:10.1002/qj.49710544504, URL
742 https://rmets.onlinelibrary.wiley.com/doi/abs/10.1002/qj.49710544504.

743 Rasmussen, E., 1985: A case study of a polar low development over the Barents Sea. *Tellus*
744 *A*, **37 (5)**, 407–418, doi:10.1111/j.1600-0870.1985.tb00440.x, URL https://doi.org/10.1111/j.
745 1600-0870.1985.tb00440.x.

746 Rasmussen, E., and A. Cederskov, 1994: Polar lows: A critical appraisal. *Proceedings of an*
747 *International Symposium on the Life Cycles of Extratropical Cyclones, Bergan, Norway.*, **111**,
748 199–203.

749 Rasmussen, E., C. Claud, and J. Purdom, 1996: Labrador Sea polar lows. *Global Atmos. Ocean*
750 *Syst*, **4**, 275–334.

Rasmussen, E., and C. Zick, 1987: A subsynoptic vortex over the Mediterranean with some resemblance to polar lows. *Tellus A*, **39A (4)**, 408–425, doi:10.1111/j.1600-0870.1987.tb00318.x, URL https://onlinelibrary.wiley.com/doi/abs/10.1111/j.1600-0870.1987.tb00318.x.

Rasmussen, E. A., and J. J. Turner, 2003: *Polar lows*. New York : Cambridge University Press, URL http://www.loc.gov/catdir/toc/cam031/2002073925.html, includes bibliographical references and index.

Reale, O., and R. Atlas, 2001: Tropical Cyclone–Like Vortices in the Extratropics: Observational Evidence and Synoptic Analysis. *Weather and Forecasting*, **16 (1)**, 7–34, doi:10.1175/1520-0434(2001)016<0007:TCLVIT>2.0.CO;2, URL https://doi.org/10.1175/1520-0434(2001)016<0007:TCLVIT>2.0.CO;2.

Reale, O., K. Lau, J. Susskind, and R. Rosenberg, 2012: AIRS impact on analysis and forecast of an extreme rainfall event (Indus River Valley, Pakistan, 2010) with a global data assimilation and forecast system. *Journal of Geophysical Research: Atmospheres*, **117 (D8)**, doi:10.1029/2011JD017093, URL https://doi.org/10.1029/2011JD017093.

Reale, O., W. Lau, J. Susskind, E. Brin, E. Liu, L. Riishojgaard, M. Fuentes, and R. Rosenberg, 2009a: AIRS impact on the analysis and forecast track of tropical cyclone Nargis in a global data assimilation and forecasting system. *Geophysical Research Letters*, **36 (6)**, doi:10.1029/2008GL037122, URL https://doi.org/10.1029/2008GL037122.

Reale, O., W. K. Lau, K.-M. Kim, and E. Brin, 2009b: Atlantic tropical cyclogenetic processes during SOP-3 NAMMA in the GEOS-5 global data assimilation and forecast system. *Journal of the Atmospheric Sciences*, **66 (12)**, 3563–3578, doi:10.1175/2009JAS3123.1, URL https://doi.org/10.1175/2009JAS3123.1.

Reale, O., E. L. McGrath-Spangler, W. McCarty, D. Holdaway, and R. Gelaro, 2018: Impact of Adaptively Thinned AIRS Cloud-Cleared Radiances on Tropical Cyclone Representation in a Global Data Assimilation and Forecast System. *Weather and Forecasting*, **33 (4)**, 909–931, doi:10.1175/WAF-D-17-0175.1, URL https://doi.org/10.1175/WAF-D-17-0175.1.

Reale, O., J. Susskind, R. Rosenberg, E. Brin, E. Liu, L. Riishojgaard, J. Terry, and J. Jusem, 2008: Improving forecast skill by assimilation of quality-controlled AIRS temperature retrievals under partially cloudy conditions. *Geophysical Research Letters*, **35 (8)**, doi:10.1029/2007GL033002, URL https://doi.org/10.1029/2007GL033002.

Reed, R. J., 1979: Cyclogenesis in Polar Air Streams. *Monthly Weather Review*, **107 (1)**, 38–52, doi:10.1175/1520-0493(1979)107<0038:CIPAS>2.0.CO;2, URL https://doi.org/10.1175/1520-0493(1979)107<0038:CIPAS>2.0.CO;2.

Reed, R. J., and C. N. Duncan, 1987: Baroclinic instability as a mechanism for the serial development of polar lows: a case study. *Tellus A: Dynamic Meteorology and Oceanography*, **39 (4)**, 376–384, doi:10.3402/tellusa.v39i4.11766, URL https://doi.org/10.3402/tellusa.v39i4.11766.

Rienecker, M., and Coauthors, 2008: The GEOS-5 Data Assimilation System–Documentation of Versions 5.0. 1, 5.1. 0, and 5.2. 0. *NASA Tech. Memo*, **104606 (27)**, 2008, URL http://gmao.gsfc.nasa.gov/pubs/docs/GEOS5_104606-Vol27.pdf.

Rojo, M., C. Claud, P.-E. Mallet, G. Noer, A. M. Carleton, and M. Vicomte, 2015: Polar low tracks over the Nordic Seas: a 14-winter climatic analysis. *Tellus A: Dynamic Meteorology and Oceanography*, **67 (1)**, 24 660, doi:10.3402/tellusa.v67.24660, URL https://doi.org/10.3402/tellusa.v67.24660.

Romero, R., and K. Emanuel, 2016: Climate Change and Hurricane-Like Extratropical Cyclones: Projections for North Atlantic Polar Lows and Medicanes Based on CMIP5 Models. *Journal of Climate*, **30 (1)**, 279–299, doi:10.1175/JCLI-D-16-0255.1, URL https://doi.org/10.1175/JCLI-D-16-0255.1.

Sardie, J. M., and T. T. Warner, 1985: A numerical study of the development mechanisms of polar lows. *Tellus A*, **37 (5)**, 460–477, doi:10.1111/j.1600-0870.1985.tb00444.x, URL https://doi.org/10.1111/j.1600-0870.1985.tb00444.x.

Singh, R., C. Kishtawal, and P. Pal, 2011: Use of atmospheric infrared sounder clear-sky and cloud-cleared radiances in the weather research and forecasting 3dvar assimilation system for mesoscale weather predictions over the indian region. *Journal of Geophysical Research: Atmospheres*, **116 (D22)**.

Spengler, T., C. Claud, and G. Heinemann, 2017: Polar Low Workshop Summary. *Bulletin of the American Meteorological Society*, **98 (6)**, ES139–ES142, doi:10.1175/BAMS-D-16-0207.1, URL https://doi.org/10.1175/BAMS-D-16-0207.1.

Susskind, J., C. Barnet, J. Blaisdell, L. Iredell, F. Keita, L. Kouvaris, G. Molnar, and M. Chahine, 2006: Accuracy of geophysical parameters derived from Atmospheric Infrared Sounder/Advanced Microwave Sounding Unit as a function of fractional cloud cover. *Journal of Geophysical Research: Atmospheres*, **111 (D9)**, doi:10.1029/2005JD006272, URL https://doi.org/10.1029/2005JD006272.

Susskind, J., C. D. Barnet, and J. M. Blaisdell, 2003: Retrieval of atmospheric and surface parameters from AIRS/AMSU/HSB data in the presence of clouds. *IEEE Transactions on Geoscience and Remote Sensing*, **41 (2)**, 390–409, doi:10.1109/TGRS.2002.808236.

Susskind, J., J. M. Blaisdell, L. Iredell, and F. Keita, 2010: Improved temperature sounding and quality control methodology using AIRS/AMSU data: The AIRS science team version 5 retrieval algorithm. *IEEE Transactions on Geoscience and Remote Sensing*, **49 (3)**, 883–907, doi:10.1109/TGRS.2010.2070508, URL https://doi.org/10.1109/TGRS.2010.2070508.

Terpstra, A., C. Michel, and T. Spengler, 2016: Forward and Reverse Shear Environments during Polar Low Genesis over the Northeast Atlantic. *Monthly Weather Review*, **144 (4)**, 1341–1354, doi:10.1175/MWR-D-15-0314.1, URL https://doi.org/10.1175/MWR-D-15-0314.1.

Tous, M., R. Romero, and C. Ramis, 2013: Surface heat fluxes influence on medicane trajectories and intensification. *Atmospheric Research*, **123**, 400–411, doi:10.1016/j.atmosres.2012.05.022, URL https://doi.org/10.1016/j.atmosres.2012.05.022.

Trahan, S., and L. Sparling, 2012: An Analysis of NCEP Tropical Cyclone Vitals and Potential Effects on Forecasting Models. *Weather and Forecasting*, **27 (3)**, 744–756, doi:10.1175/WAF-D-11-00063.1, URL https://doi.org/10.1175/WAF-D-11-00063.1.

Verezemskaya, P., N. Tilinina, S. Gulev, I. A. Renfrew, and M. Lazzara, 2017: Southern Ocean mesocyclones and polar lows from manually tracked satellite mosaics. *Geophysical Research Letters*, **44 (15)**, 7985–7993, doi:10.1002/2017GL074053, URL https://agupubs.onlinelibrary.wiley.com/doi/abs/10.1002/2017GL074053.

Wang, P., J. Li, Z. Li, A. H. Lim, J. Li, T. J. Schmit, and M. D. Goldberg, 2017: The impact of cross-track infrared sounder (cris) cloud-cleared radiances on hurricane joaquin (2015) and matthew (2016) forecasts. *Journal of Geophysical Research: Atmospheres*, **122 (24)**, 13–201.

Watanabe, S.-i. I., H. Niino, and W. Yanase, 2016: Climatology of Polar Mesocyclones over the Sea of Japan Using a New Objective Tracking Method. *Monthly Weather Review*, **144 (7)**, 2503–

838 2515, doi:10.1175/MWR-D-15-0349.1, URL https://doi.org/10.1175/MWR-D-15-0349.1.

839 White, R. H., D. S. Battisti, and G. H. Roe, 2017: Mongolian Mountains Matter Most: Impacts
840 of the Latitude and Height of Asian Orography on Pacific Wintertime Atmospheric Circulation.
841 *Journal of Climate*, **30 (11)**, 4065–4082, doi:10.1175/JCLI-D-16-0401.1, URL https://doi.org/
842 10.1175/JCLI-D-16-0401.1.

843 Wu, L., S. A. Braun, J. J. Qu, and X. Hao, 2006: Simulating the formation of Hurricane Isabel
844 (2003) with AIRS data. *Geophysical Research Letters*, **33 (4)**, doi:10.1029/2005GL024665,
845 URL https://doi.org/10.1029/2005GL024665.

846 Wu, W.-S., R. J. Purser, and D. F. Parrish, 2002: Three-dimensional variational analysis with
847 spatially inhomogeneous covariances. *Monthly Weather Review*, **130 (12)**, 2905–2916.

848 Xia, L., M. Zahn, K. Hodges, F. Feser, and H. Storch, 2012: A comparison of two identification
849 and tracking methods for polar lows. *Tellus A: Dynamic Meteorology and Oceanography*, **64 (1)**,
850 17 196, doi:10.3402/tellusa.v64i0.17196, URL https://doi.org/10.3402/tellusa.v64i0.17196.

851 Yanase, W., H. Niino, S.-i. I. Watanabe, K. Hodges, M. Zahn, T. Spengler, and I. A. Gurvich,
852 2016: Climatology of Polar Lows over the Sea of Japan Using the JRA-55 Reanalysis. *Journal*
853 *of Climate*, **29 (2)**, 419–437, doi:10.1175/JCLI-D-15-0291.1, URL https://doi.org/10.1175/
854 JCLI-D-15-0291.1.

855 Zappa, G., L. Shaffrey, and K. Hodges, 2014: Can Polar Lows be Objectively Identified and Tracked
856 in the ECMWF Operational Analysis and the ERA-Interim Reanalysis? *Monthly Weather*
857 *Review*, **142 (8)**, 2596–2608, doi:10.1175/MWR-D-14-00064.1, URL https://doi.org/10.1175/
858 MWR-D-14-00064.1.

Zhou, Y. P., K.-M. Lau, O. Reale, and R. Rosenberg, 2010: AIRS impact on precipitation analysis and forecast of tropical cyclones in a global data assimilation and forecast system. *Geophysical Research Letters*, **37 (2)**, doi:https://doi.org/10.1029/2009GL041494, URL https://agupubs.onlinelibrary.wiley.com/doi/abs/10.1029/2009GL041494.

LIST OF FIGURES

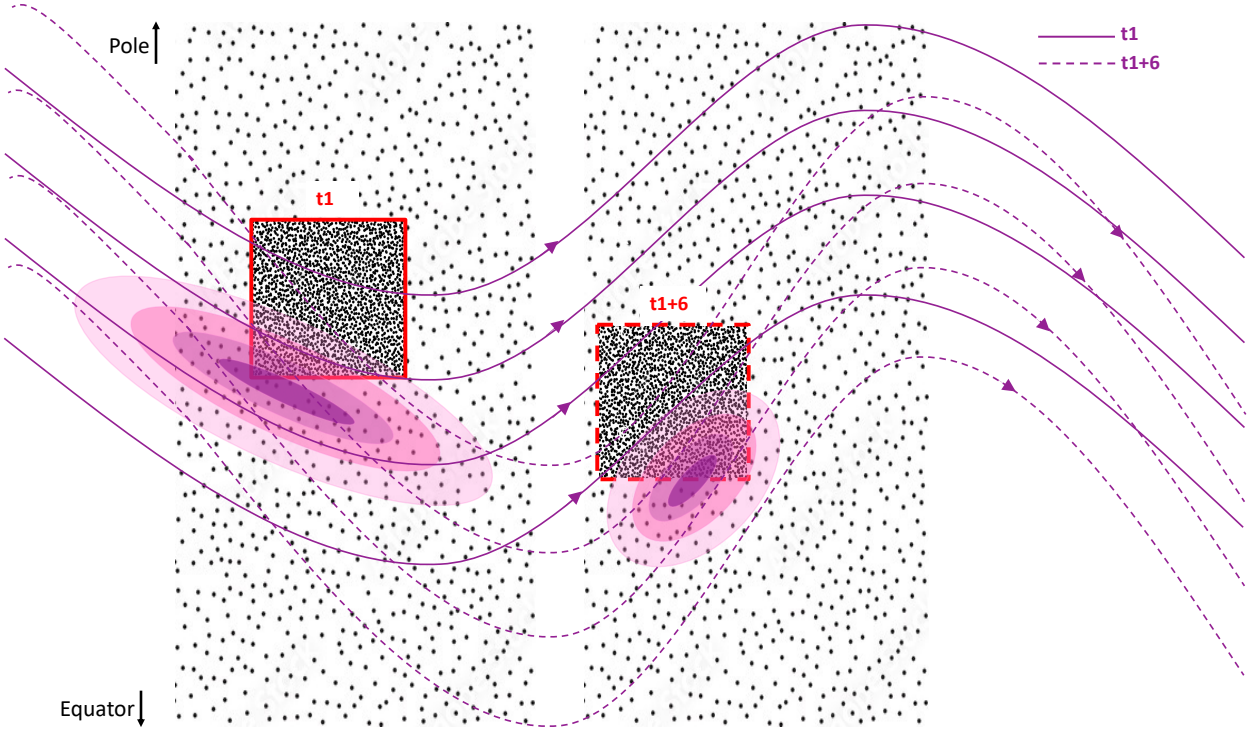

FIG. 1. Conceptual representation of feature-based adaptive thinning of AIRS radiances. In this case, the adaptive thinning domain follows the highest velocity gradients associated with a jet speed maximum (shaded ellipse) at times 't1' and 't1+6' hours in the analysis. The jet is represented by purple streamlines at times t1 (solid) and t1+6 (dashed) hours, respectively. A moving domain (red box) is activated on the cylonically sheared side of the jet speed maximum, encompassing the poleward side of the region with strongest horizontal velocity gradients, at times t1 (red solid) and t1+6 (red dashed) hours, respectively. AIRS radiances are assimilated at 145 km x 145 km density inside the moving domain, as indicated by the dense black dots, whereas a thinning level of 300 km (about 1/4th density) is used for assimilation outside the domain (sparse black dots).

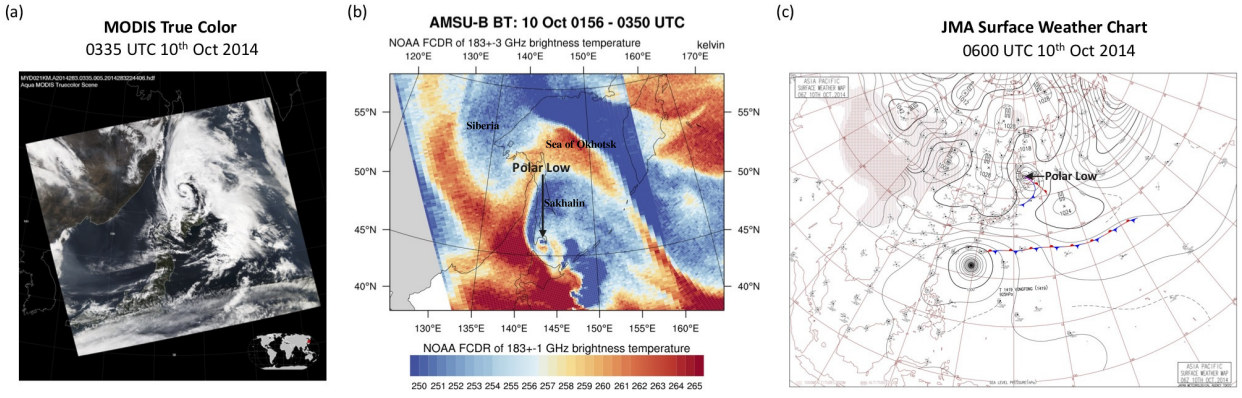

953 FIG. 2. Observations of spiral cloud over the Sea of Okhotsk from (a) MODIS true color image and (b)
954 AMSU-B/MHS 183.3 GHz brightness temperatures (K); (c) surface weather chart analysis on 10 October 2014.
955 *"JMA Surface Weather Chart" (from the Japan Meteorological Agency website).*

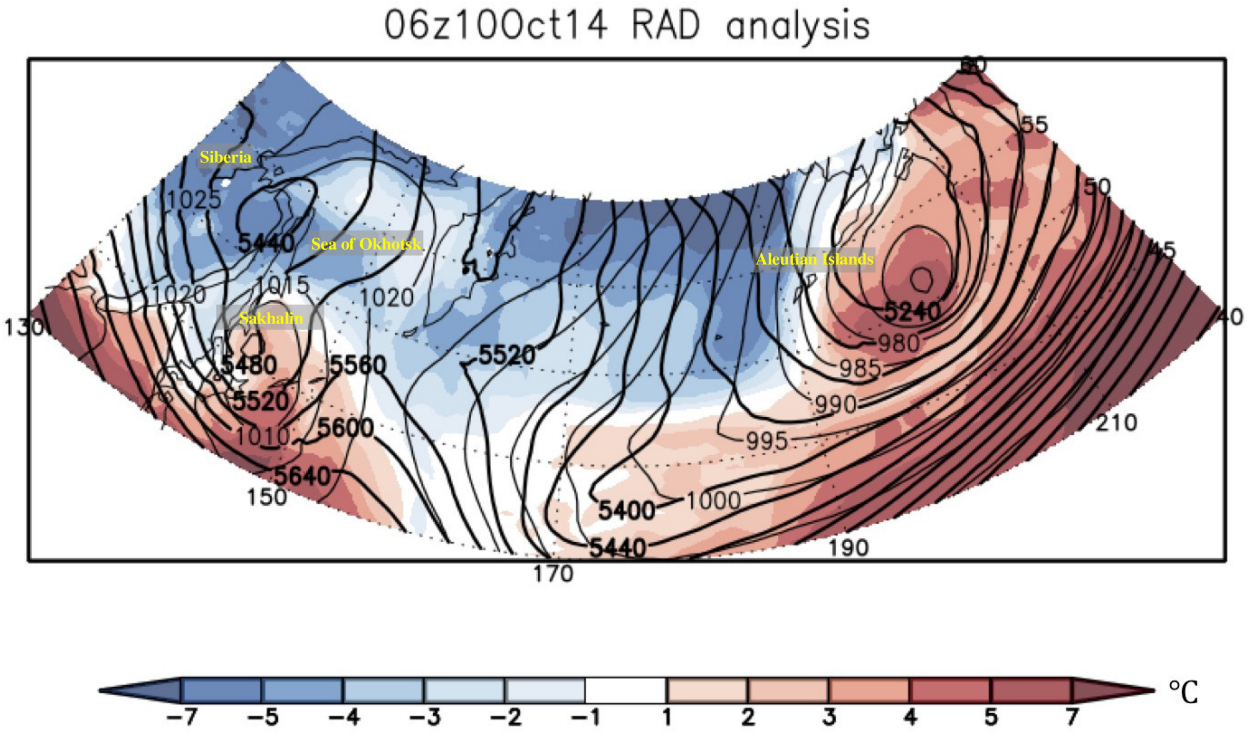

956 FIG. 3. The 850hPa temperature (°C; shaded), sea-level pressure (hPa; thin contour), and 500hPa geopotential
957 height (meters; thick contour) observed at 06z 10 October 2014 in the RAD analysis.

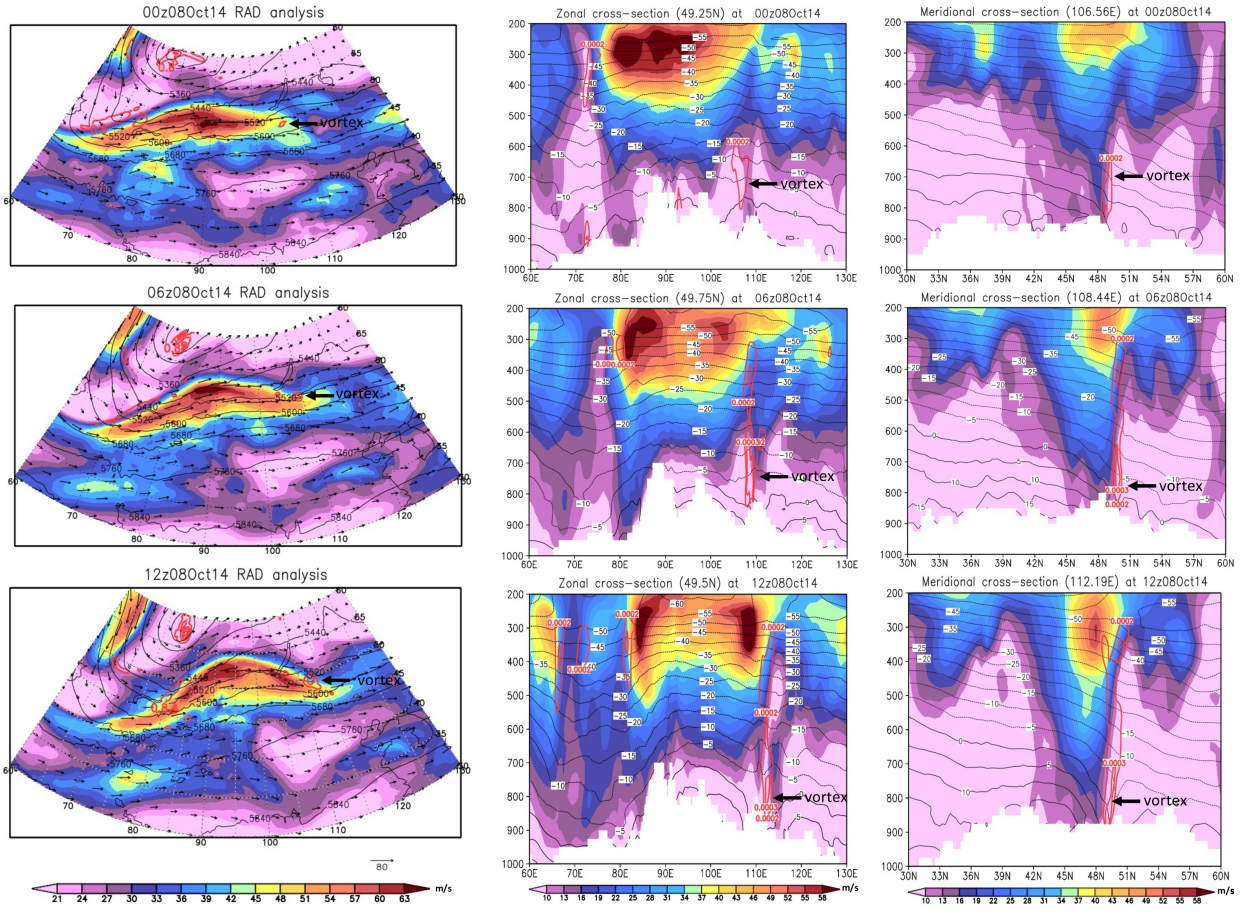

958 FIG. 4. (left) The 250hPa wind vector (arrows) and wind speed ($m\,s^{-1}$; shaded), 500hPa geopotential height
959 (meters; black contour), and the vertically integrated vorticity from surface to 300hPa ($kg\,m^{-2}\,s^{-1}$; red contour)
960 showing the origin of the mesoscale vortex in RAD analysis; (center) longitude-height and (right) latitude-height
961 cross-section of the vortex showing wind speed ($m\,s^{-1}$; shaded), temperature (°C; black contour), and vorticity
962 (s^{-1}; red contour).

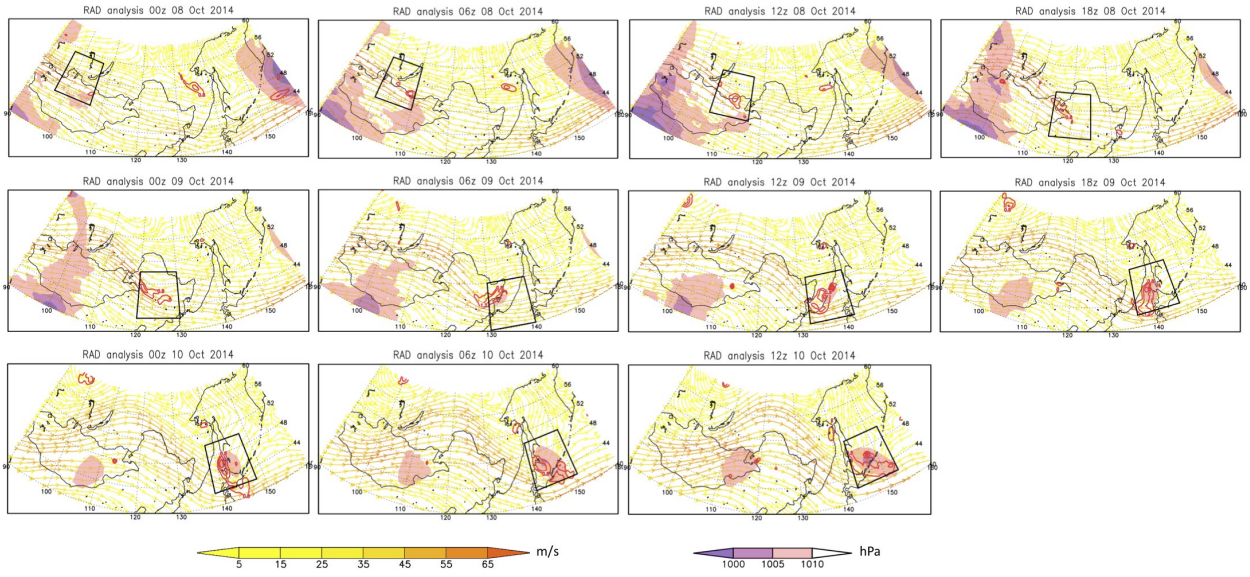

963 FIG. 5. The 250hPa streamlines ($m\,s^{-1}$; yellow shaded), sea level pressure (hPa; shaded contours), and the
964 vertically integrated vorticity from surface to 300hPa ($kg\,m^{-2}\,s^{-1}$; red contour) in the 6-hourly RAD analysis
965 from 00z 08 October to 12z 10 October 2014. The PL domain used for adaptive thinning of AIRS CCRs is
966 shown in black.

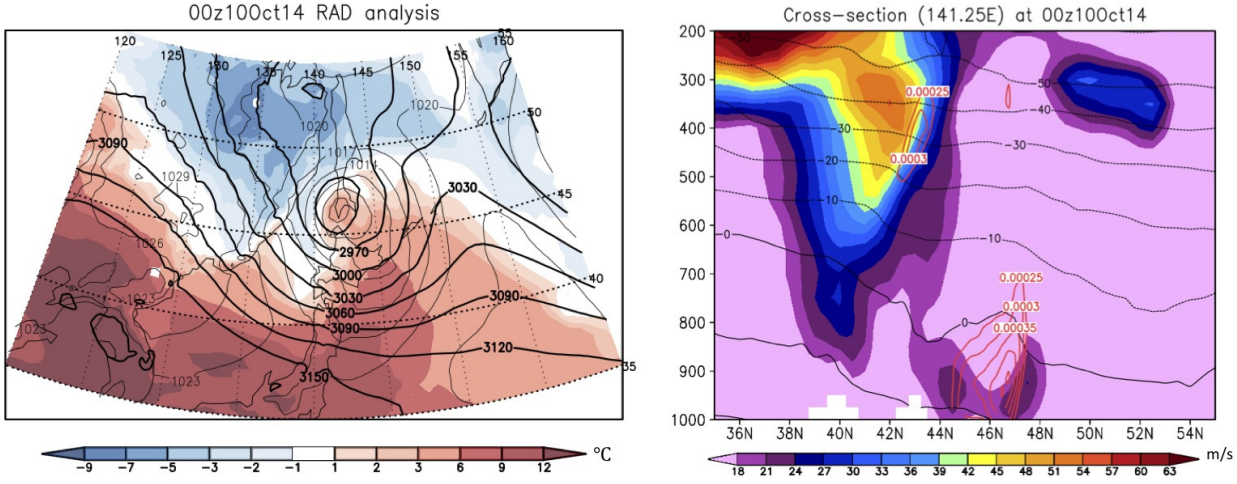

Fig. 6. (left) The 850hPa temperature (°C; shaded), sea-level pressure (hPa; thin black contour), and 700 hPa geopotential height (meters; thick black contour) observed at 00z 10 October 2014 in the RAD analysis showing an occluded mesoscale front, and (right) latitude-height cross-section of wind speed (m s^{-1}; shaded), temperature (°C; black contour), and vorticity (s^{-1}; red contour) showing the incipient polar low.

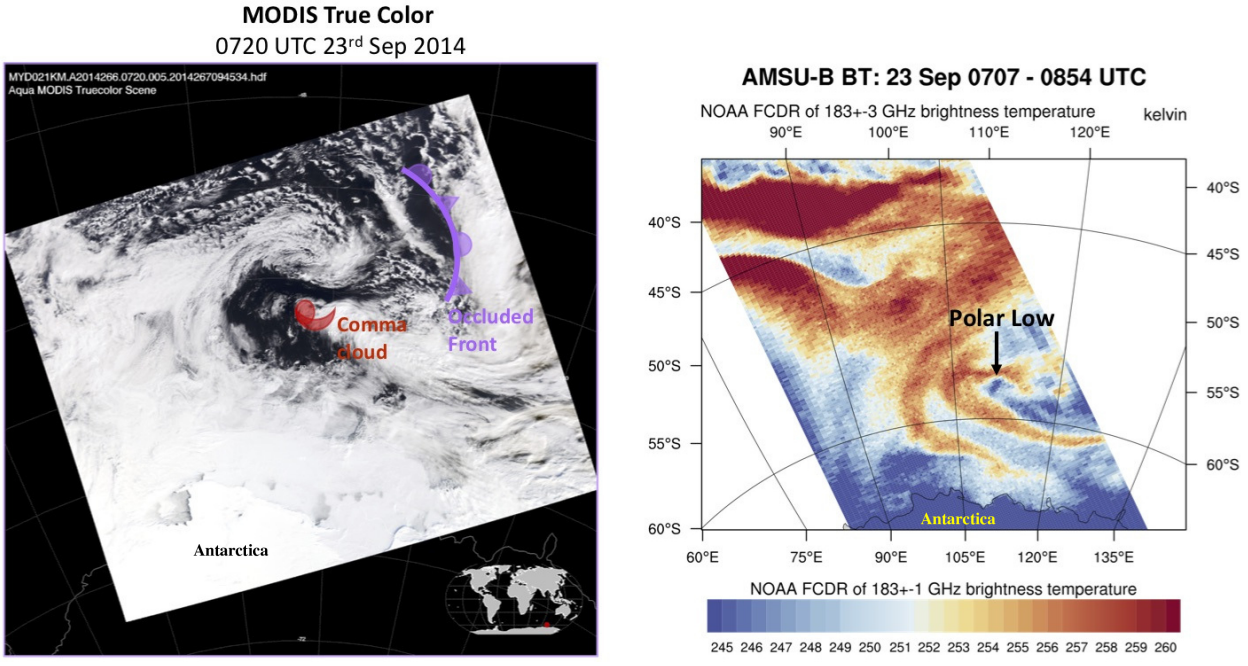

971 FIG. 7. Observations of comma cloud over the Southern Ocean from (left) MODIS true color image (also
972 showing the cloud field associated with an occluded front) and (right) AMSU-B/MHS 183.3 GHz brightness
973 temperatures (K) on 23 September 2014.

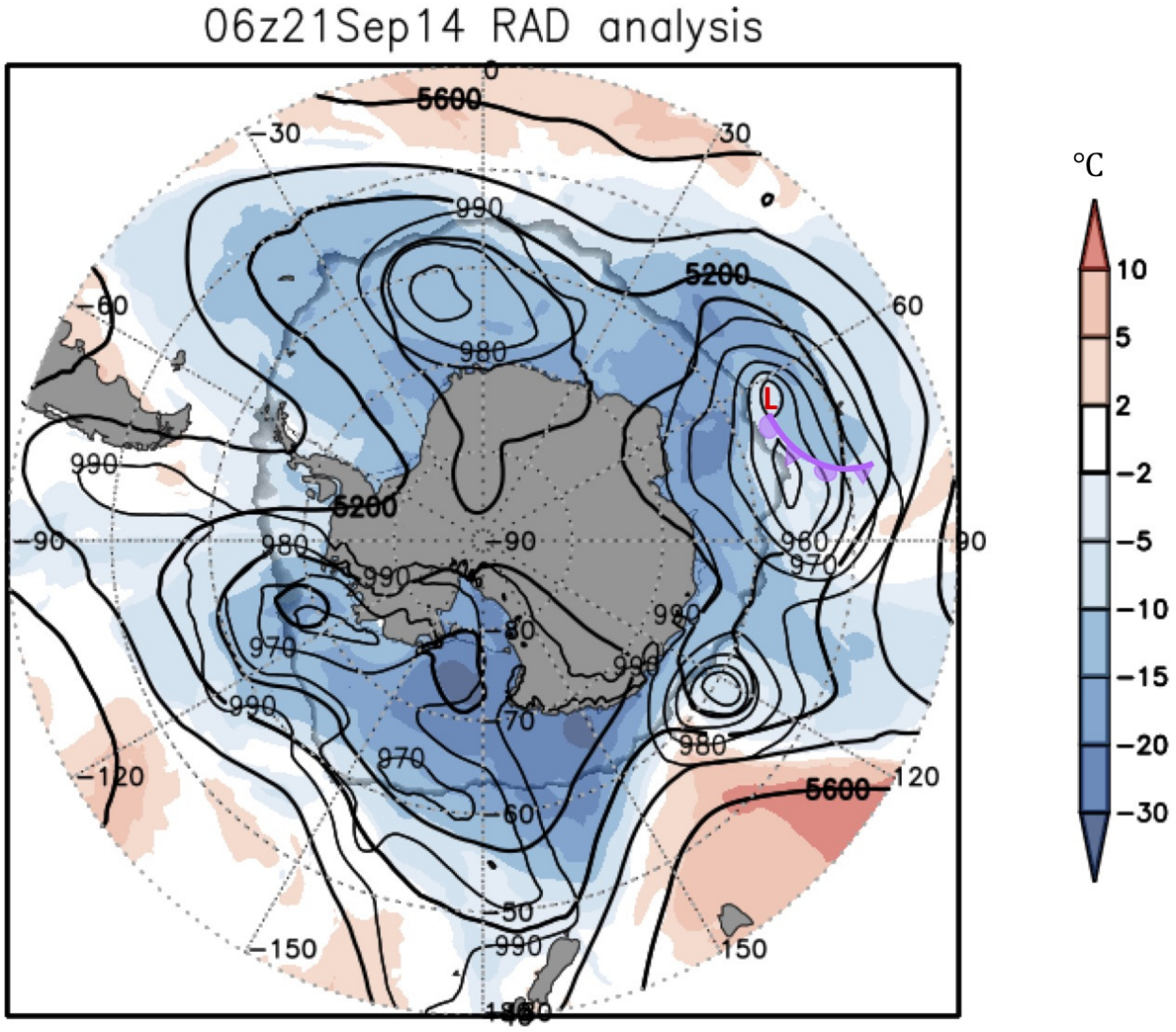

974 FIG. 8. The 850hPa temperature (°C; shaded), sea-level pressure (hPa; thin black contour), 500mb geopotential
975 height (meters; thick black contour) at 06z 21 September 2014 in the RAD analysis. The sea ice margin (defined
976 as sea ice fraction ranging between 0.5 to 0.15) is indicated by grey contours. The occluded front is indicated in
977 purple, and the associated surface low is indicated by the letter "L" in red.

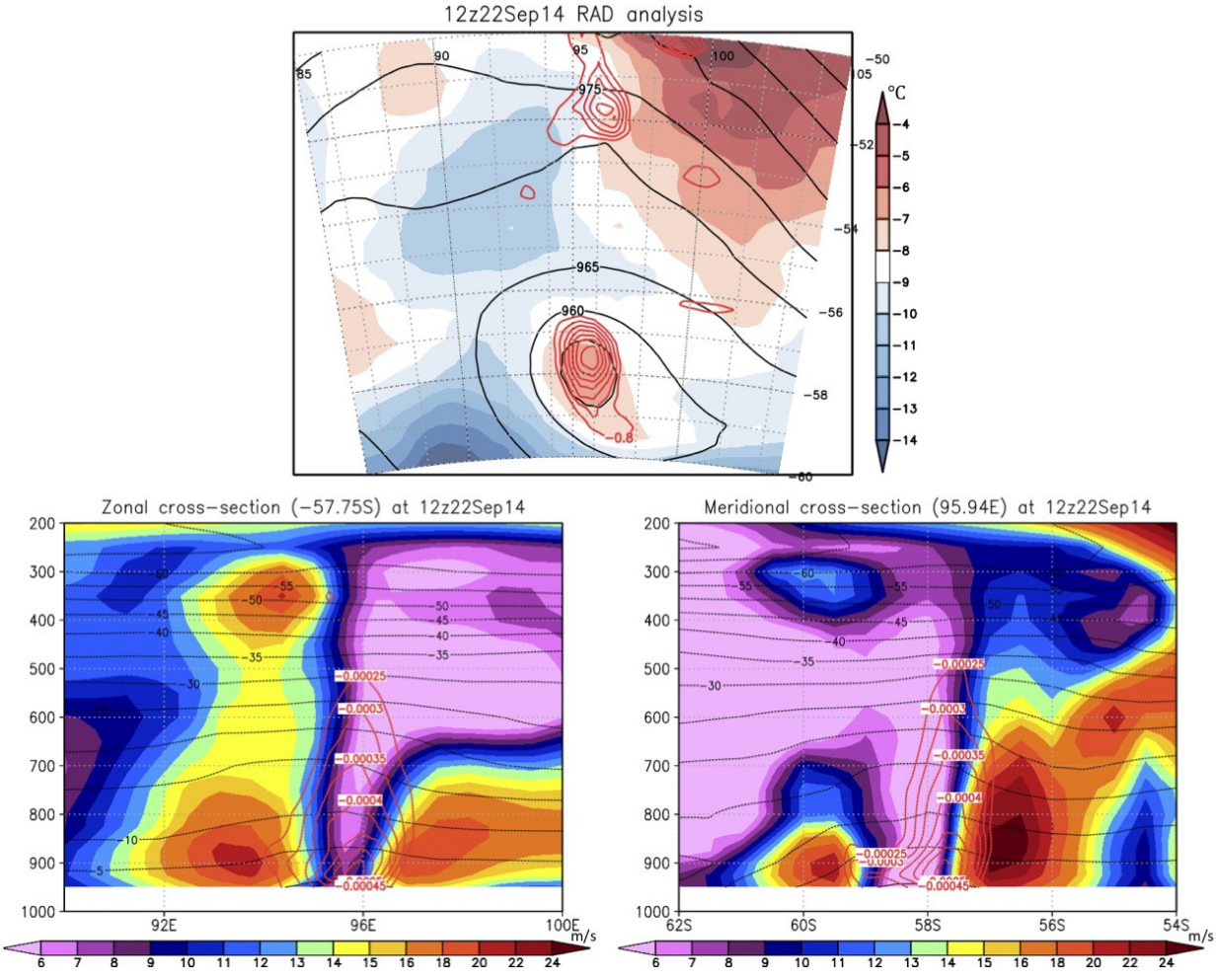

978 FIG. 9. (top) The 850hPa temperature (°C; shaded), sea-level pressure (hPa; black contour), and vertically
979 integrated vorticity from surface to 300hPa (kg m^{-2} s^{-1}; red contour) observed at 12z 22 September 2014 during
980 the mature phase of the spurious low in the RAD analysis (not observed), and (bottom) vertical cross-sections of
981 the wind speed (m s^{-1}; shaded), temperature (°C; black contour), and vorticity (s^{-1}; red contour) across the core
982 of the spurious low.

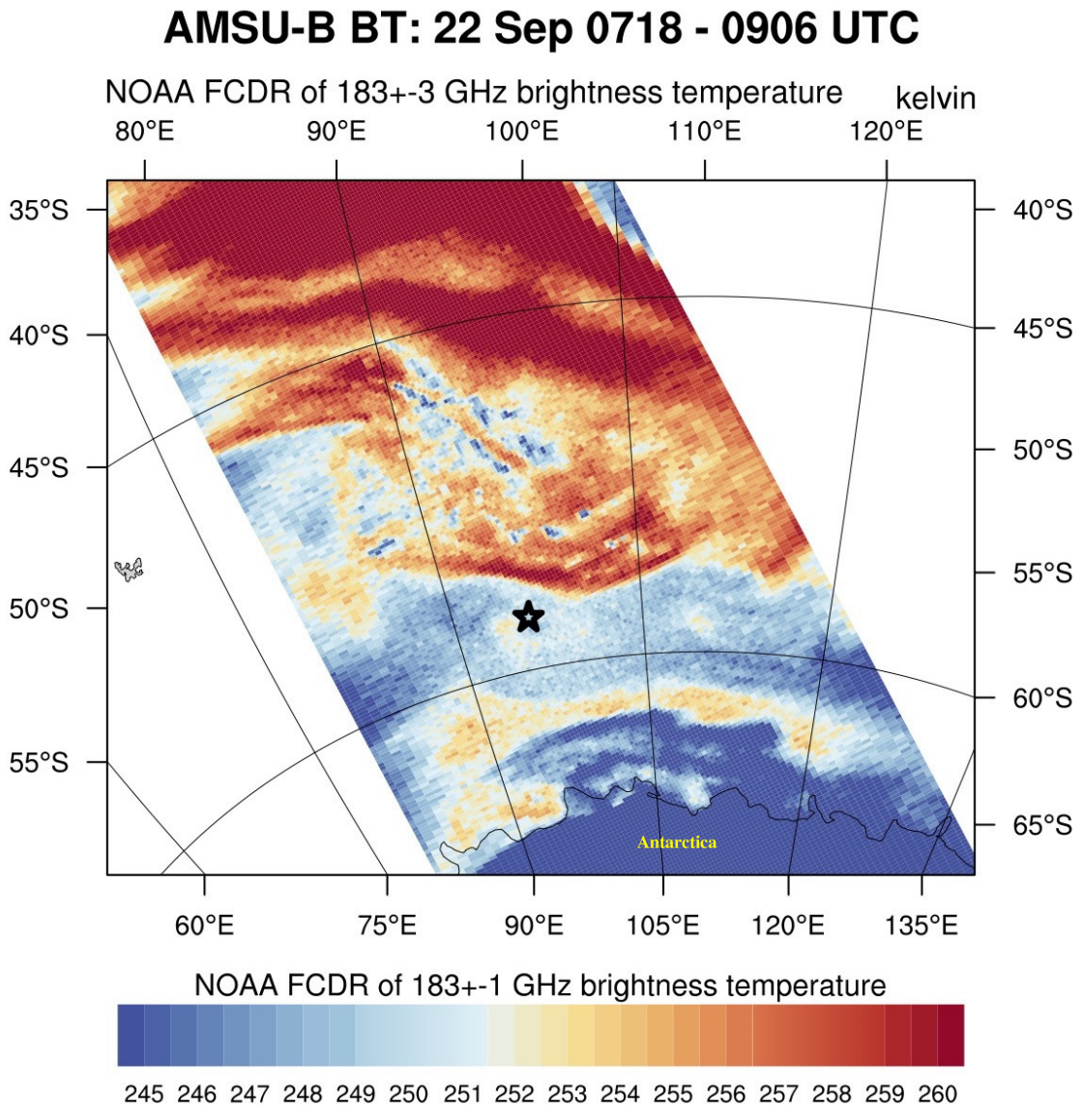

983 FIG. 10. The AMSU-B/MHS 183.3 GHz brightness temperatures (K) observations between 0718-0906 UTC
984 22 September 2014, confirming the absence of convective clouds. The black star indicates the position of the
985 spurious low (false positive) in the RAD analysis at this time.

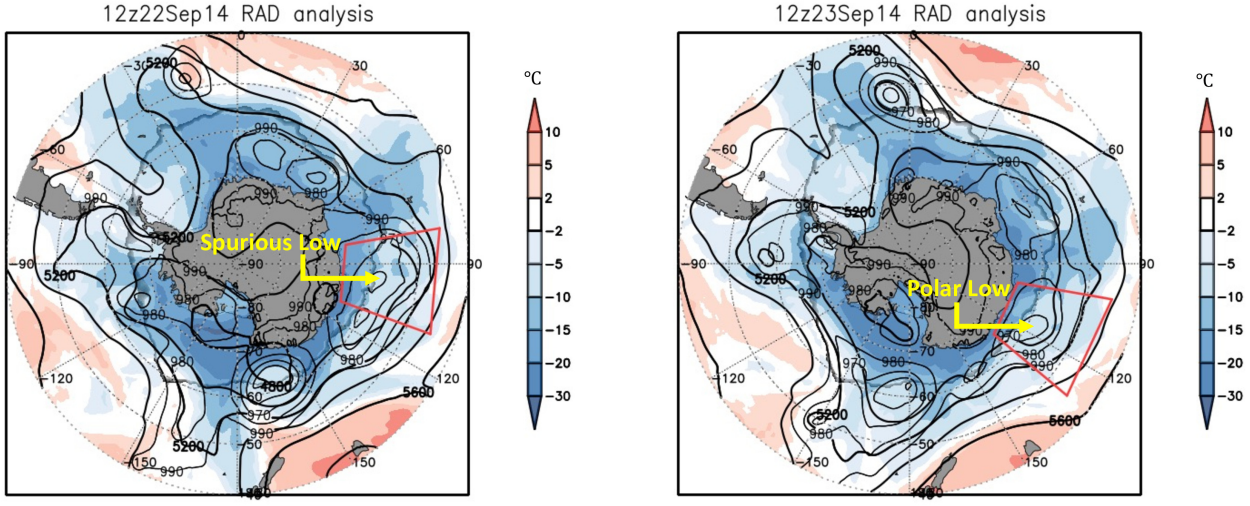

986 FIG. 11. As in Figure 8 but for (left) 12z 22 September and (right) 12z 23 September 2014. The position of
987 the spurious low (not observed) and Polar Low (observed) in RAD analysis is indicated, and the PL domain used
988 for adaptive thinning of AIRS CCRs is shown in red.

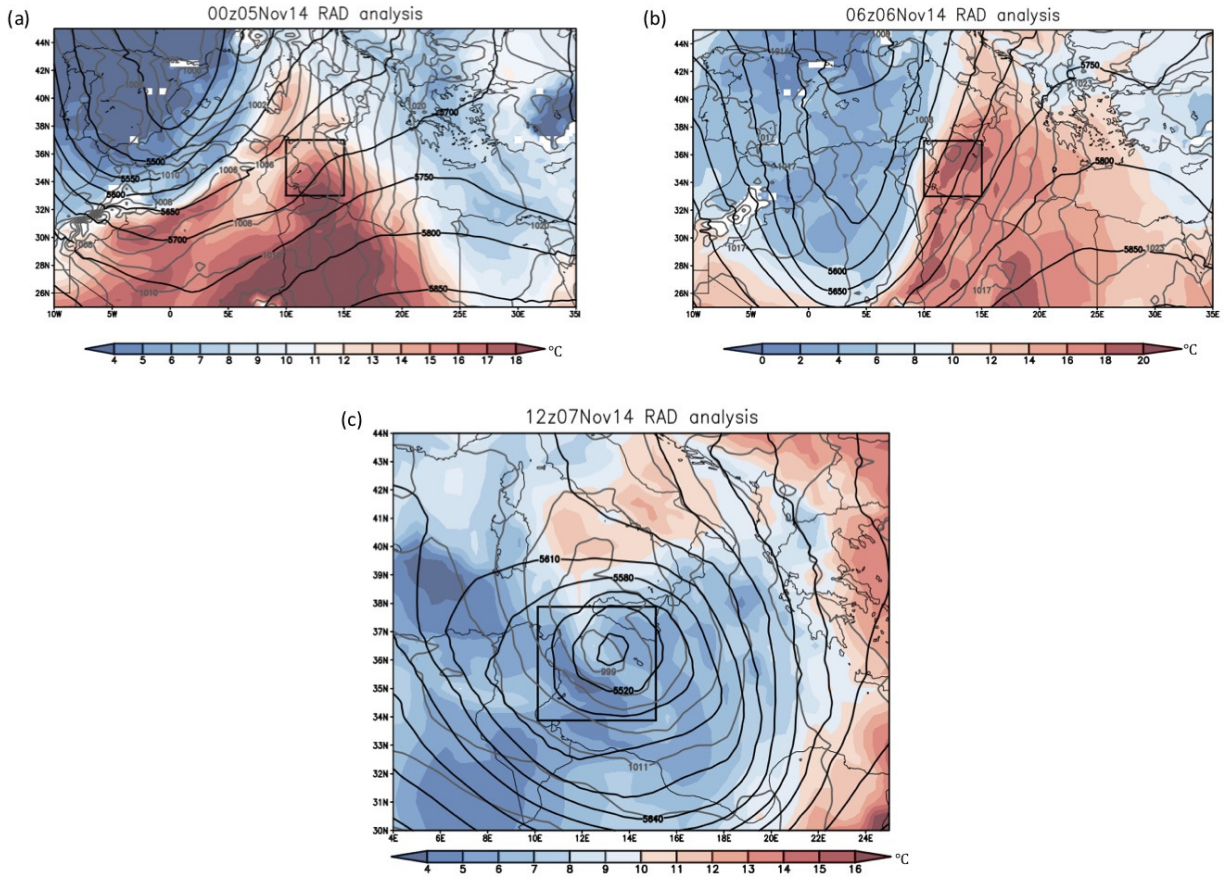

989 FIG. 12. The 850hPa temperature (°C; shaded), sea-level pressure (hPa; grey contour), and 500 hPa geopotential
990 height (meters; black contour) observed at (a) 00z 05 November 2014 showing a mesoscale surface low along
991 the edge of a warm front, (b) 06z 06 November 2014 showing a mesoscale surface low along the edge of a cold
992 front, and (c) 12z 07 November 2014 showing an occluded front marking the genesis of T-LC Qendresa in the
993 RAD analysis. The black box shows the PL domain used for adaptive thinning of AIRS CCRs.

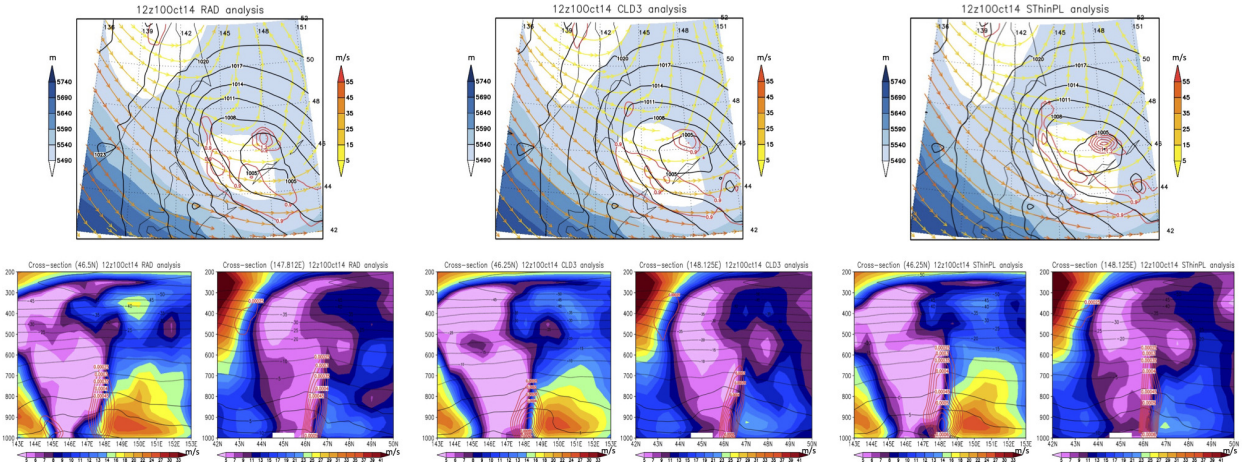

FIG. 13. (top) The 250hPa streamlines ($m\,s^{-1}$; yellow shaded), 500hPa geopotential heights (meters; blue shaded), sea-level pressure (hPa; black contour), and vertically integrated vorticity from surface to 300hPa ($kg\,m^{-2}\,s^{-1}$; red contour) as observed in model analyses at 12z 10 October 2014 (time of peak intensity of the Okhotsk Sea PL) and (bottom) zonal and meridional cross-sections of wind speed ($m\,s^{-1}$; shaded), temperature (°C; black contour), and vorticity (s^{-1}; red contour) across the PL core.

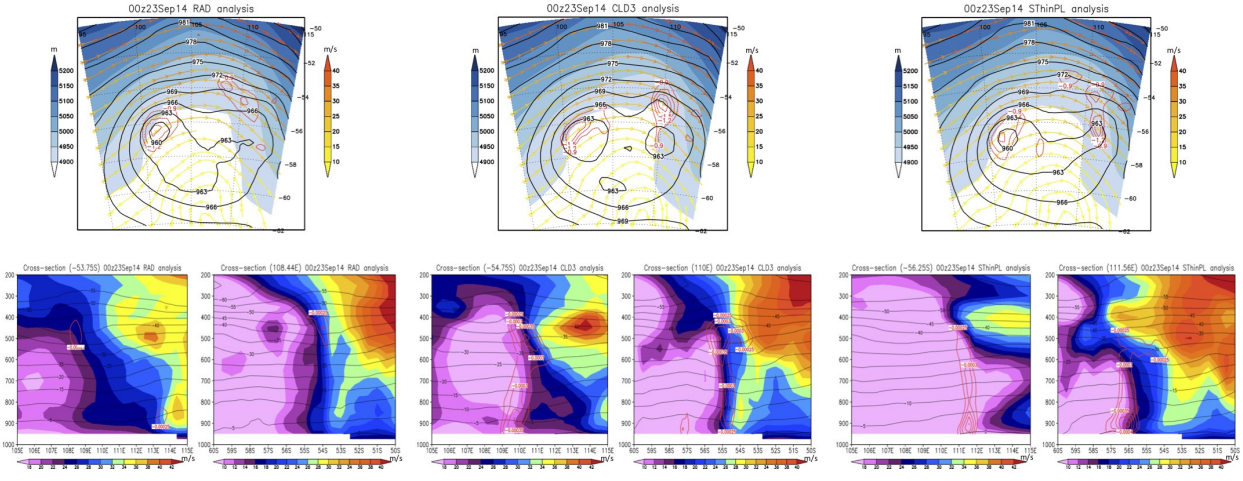

FIG. 14. (top) The 250hPa streamlines ($m\,s^{-1}$; yellow shaded), 500hPa geopotential heights (meters; blue shaded), sea-level pressure (hPa; black contour), and vertically integrated vorticity from surface to 300hPa ($kg\,m^{-2}\,s^{-1}$; red contour) as observed in model analyses during the genesis phase of the Southern Ocean PL, and (bottom) zonal and meridional cross-sections of wind speed ($m\,s^{-1}$; shaded), temperature (°C; black contour), and vorticity (s^{-1}; red contour) across the vortex.

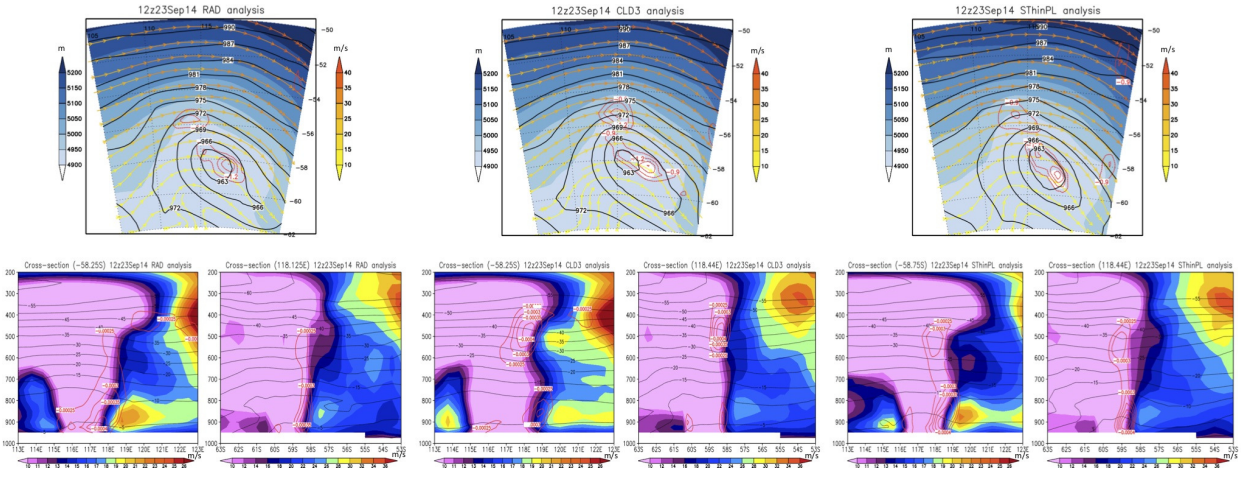

FIG. 15. (top) The 250hPa streamlines ($\mathrm{m\,s^{-1}}$; yellow shaded), 500hPa geopotential heights (meters; blue shaded), sea-level pressure (hPa; black contour), and vertically integrated vorticity from surface to 300hPa ($\mathrm{kg\,m^{-2}\,s^{-1}}$; red contour) as observed in model analyses at 12z 23 September 2014 (time of peak intensity of the Antarctic PL) , and (bottom) zonal and meridional cross-sections of wind speed ($\mathrm{m\,s^{-1}}$; shaded), temperature (°C; black contour), and vorticity ($\mathrm{s^{-1}}$; red contour) across the vortex

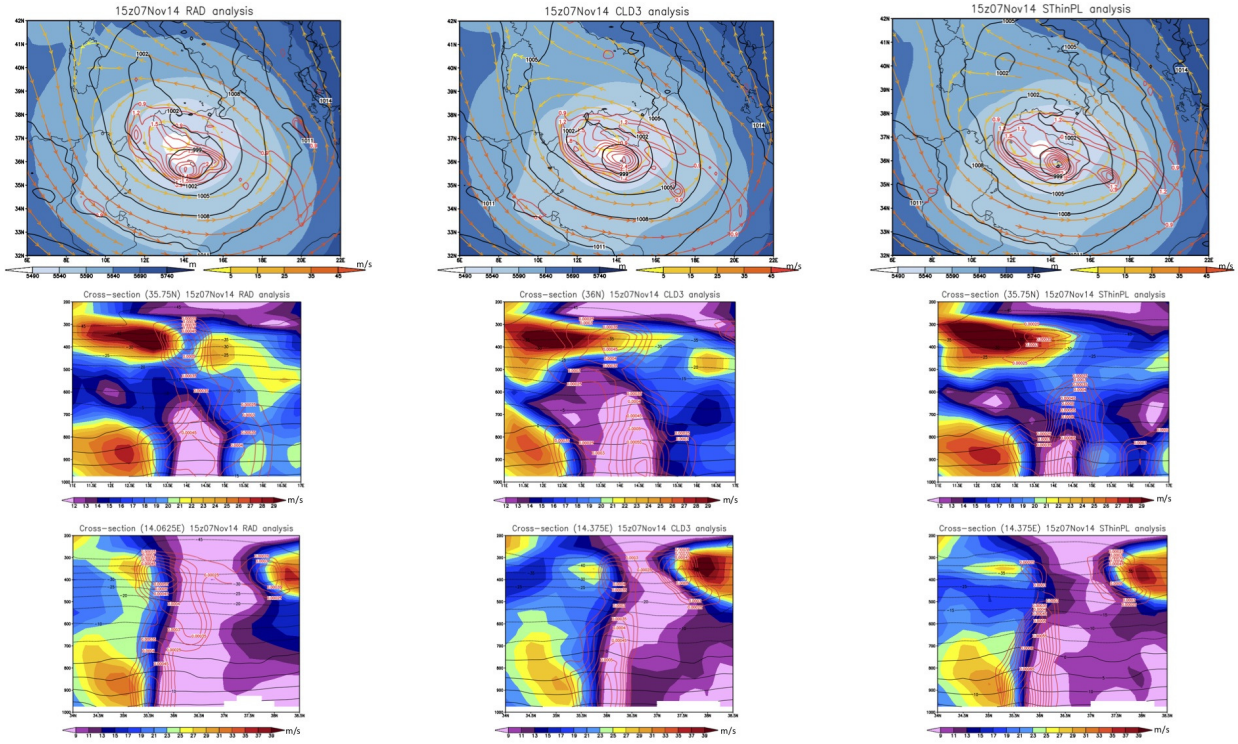

FIG. 16. (top) The 250hPa streamlines ($m\,s^{-1}$; yellow shaded), 500hPa geopotential heights (meters; blue shaded), sea-level pressure (hPa; black contour), and vertically integrated vorticity from surface to 300hPa ($kg\,m^{-2}\,s^{-1}$; red contour) as observed in model experiments prior to landfall at Malta, and (bottom) zonal and meridional cross-sections of wind speed ($m\,s^{-1}$; shaded), temperature (°C; black contour), and vorticity (s^{-1}; red contour) across the T-LC core.